

Determining the Physical Properties of the B Stars II. Calibration of Synthetic Photometry

E.L. Fitzpatrick¹, D. Massa²

ABSTRACT

We present a new calibration of optical (*UBV*, Strömgren *uvby β* , and Geneva) and near IR (Johnson *RIJHK* and *2MASS*) photometry for B and early A stars derived from Kurucz (1991) *ATLAS9* model atmospheres. Our sample of stars consists of 45 normal, nearby B and early A stars which have high quality, low resolution *IUE* spectra and accurate *Hipparcos* parallaxes. The calibration is unique because it relies *only* on the UV spectral energy distributions, the absolute flux calibration of the *V* filter and the *Hipparcos* distances to determine the appropriate model atmospheres for the program stars. These models are then used to calibrate the synthetic photometry. We compare our results with previous, well accepted results and provide a thorough discussion of the random errors and systematic effects affecting the calibration. In particular, we demonstrate the influence of $v \sin i$ on surface gravities derived from fitting model atmospheres. Finally, we discuss some of our intended applications of this new calibration.

Subject headings:

1. Introduction

We have begun a detailed study of Galactic B and early-A main sequence stars, whose goals are to both derive detailed measurements of the basic physical properties of these stars (along with ancillary information such as distance and interstellar extinction characteristics) and to critically test the current atmosphere and interior models which provide the transformation between observable quantities and the stellar properties, as well as yielding insight into the structure and evolution of these stars.

The B and early-A main sequence stars play a central role in many stellar astrophysics studies. Simply put, they are the most massive and luminous objects whose atmospheres are well-represented

¹Department of Astronomy & Astrophysics, Villanova University, Villanova, PA 19085, USA; fitz@astronomy.villanova.edu

²SGT, Inc., NASA/GSFC, Mailstop 681.0, Greenbelt, MD 20771; massa@derckmassa.net

by the simplifying assumptions of LTE physics, hydrostatic equilibrium, and plane-parallel geometry. Thus, precise determinations of their individual properties should be possible through the application of currently available and well-developed astrophysical tools. Because the evolutionary histories of these objects are generally simple (e.g., unaffected by significant mass loss) the interpretation of their properties — particularly their surface compositions — is straightforward. The potential applications of such results are manifold, including tests of stellar structure and evolution predictions, distance determinations, galactic chemical composition studies, and the investigation of the physical processes responsible for chemical peculiarities (notably among the late-B and A types). Moreover, since the analyses of more massive and/or more evolved objects are much more physically and computationally challenging (requiring the inclusion of NLTE physics, dynamical effects, and evolutionary modifications of their surface abundances), the results for main sequence B and A stars associated with more massive stars — as in a cluster — provide the essential benchmarks for interpreting the results for the more luminous objects.

As initial steps in this program, we have demonstrated how low-resolution UV and optical spectral energy distribution (SED) observations, when combined with the predictions of stellar atmosphere models, can provide excellent estimates of the basic properties of A or B stars (see Fitzpatrick & Massa 1999, hereafter FM). Specifically, we showed how the SED determines the effective temperature, T_{eff} ; surface gravity, $\log g$; the abundance of Fe-group elements, $[Fe/H]$; and the magnitude of the microturbulent velocity field in the atmosphere, v_{turb} . This methodology was then applied to a number of eclipsing binary systems in both the Milky Way and Large Magellanic Cloud (Guinan et al. 1998, 2000; Ribas et al. 2000, 2002; and Fitzpatrick et al. 2002, 2003). These results verified that the *ATLAS9* (Kurucz 1991) model atmospheres provide excellent representations of the UV and optical SEDs of B and A stars and yield reliable estimates of the stellar properties. Recently, Niemczura (2003) applied the FM methodology to slowly pulsating B stars, deriving important results on the lack of metallicity-dependence of the pulsation phenomenon.

For a few stars, spectrophotometric observations covering the entire UV-through-optical spectral domain (where B and A stars emit from 70-to-100% of their energy) are available from spectrometers aboard the *Hubble Space Telescope* (*HST*). These high-precision, long wavelength baseline, and absolutely calibrated data (see Bohlin 1986), make the comparison between observations and model predictions straightforward. Since both are expressed in flux units, all one has to do is match the spectral resolution of the observed SEDs with the theoretical models. However, to expand our study to encompass large numbers of stars, we must tap other observational resources. The primary stellar SED datasets currently available are low-resolution *International Ultraviolet Explorer* (*IUE*) spectrophotometry (covering the range 1165-3000 Å), optical *UBV*, *uvby β* , and Geneva photometry, and near-IR *JHK* photometry from the *2MASS* project. To allow these data to be compared with model atmosphere predictions, the *IUE* observations must be absolutely calibrated and the synthetic photometric indices derived from the models must be transformed to the observational systems. The first of these tasks was completed by Massa & Fitzpatrick (2000), and this paper addresses the second.

Several calibrations of synthetic optical photometry already exist. Relyea & Kurucz (1978) relied on a single star with known physical properties to calibrate their synthetic *uvby* photometry, while Balona (1984) used the Code et al. (1976) sample of stars with known angular diameters and temperatures determined from UV SEDs to calibrate his model *uvby β* photometry. Moon & Dworetzky (1985) used these same stars, supplemented by other stars whose physical properties were known from either model atmosphere analyses or eclipsing binary observations. In this way, they extended the range of the calibration and refined its accuracy. Later, Napiwotzki et al. (1993, hereafter NSW) employed the Code et al. sample, with the *OAO-2* fluxes recalibrated by Beeckmans (1977), together with A and F stars whose T_{eff} and $\log g$ values were derived from model atmosphere fits to *TD-1* observations by Malagnini et al. (1982) and lightly reddened B5 – A0 stars whose physical properties were determined from fits to a combination of *TD-1* data and optical spectrophotometry by Malagnini et al. (1983). Geneva photometry has been previously calibrated by Künzli, et al. (1997), among others, and so has the Johnson *RIJHK* photometric system (e.g., Bessell et al. 1998) and *2MASS* (Cohen et al. 2003).

While the goal of this paper is to produce yet another calibration of synthetic optical and near-IR photometry from the Kurucz *ATLAS9* models, our approach is unique. Consequently, it provides a valuable independent verification of previous calibrations and also presents its own distinct advantages. Unlike other calibrations, we determine the interstellar extinction and *all* of the physical properties of each program star (T_{eff} , $\log g$, [m/H], and v_{turb}) by fitting the details of its *IUE* UV SED (corrected and placed on the *HST* FOS system using the Massa & Fitzpatrick 2000, hereafter MF, results) and its *V* magnitude to an *ATLAS9* model. Furthermore, the properties of each star are constrained by a combination of the observed *Hipparcos* distance to the star and stellar interior models. The best fitting *ATLAS9* model for each star is then used to calculate its synthetic photometry. Finally, the synthetic model photometry of all the program stars is fit to their observed photometry in order to derive the transformations. The advantages of this approach are that it utilizes more spectral information than previous calibrations (allowing an unambiguous determination of the physical properties for each star), and that it incorporates independent, non-spectroscopic ancillary data directly into the calibration process. In addition, this calibration provides the most internally consistent transformation when UV SEDs and optical and near-IR photometry are fit simultaneously.

In the sections below, we begin with a general discussion of our calibration strategy (§ 2), followed by a description of the main ingredients in the analysis, i.e., the sample of stars and the adopted grid of stellar atmosphere models (§ 3). We then, in § 4, present the results of the model-fitting procedure and assess the internal sources of error. We describe how the synthetic photometry is calibrated in § 5 and present the final catalog of calibrated synthetic photometry in § 6. In § 7, we compare the calibrated data to other, currently available calibrations, assess possible sources of systematic errors, and describe how to apply the calibrated photometry. Finally, in § 8, we summarize our results and highlight several potential applications.

2. Overview of the Photometric Calibration

Our calibration of synthetic photometry involves three steps: First, we find the reddened and distanced-attenuated stellar atmosphere models which best match the observed SEDs of our program stars, as described below. Second, we perform synthetic optical and near-IR photometry on the models for each program star to obtain a set of uncalibrated synthetic photometric magnitudes and indices for each star. Third, we compare the synthetic photometry with the observed photometry, to determine the transformations between the observed and synthetic systems. This latter step is essentially identical to that performed in standard photometric reductions, where instrumental values are transformed to a calibrated standard system.

We model the shapes of the stellar SEDs as follows. Let f_λ be the SED of a star as observed from Earth. It depends on the surface flux of the star and on the attenuating effects of distance and interstellar extinction and can be expressed as

$$f_\lambda = F_\lambda \times \left(\frac{R}{d}\right)^2 \times 10^{-0.4E(B-V)[k(\lambda-V)+R(V)]} \quad (1)$$

where F_λ is the surface flux, R is the stellar radius, and d is the distance. The last term carries the extinction information, including $E(B - V)$, the normalized extinction curve $k(\lambda - V) \equiv E(\lambda - V)/E(B - V)$, and the ratio of selective-to-total extinction in the V band $R(V) \equiv A_V/E(B - V)$. We use the MPFIT procedure by Craig Markwardt to determine the optimal values of all the parameters which contribute to the righthand side of equation 1, and thus to achieve the best fit to the observed fluxes f_λ (see Markwardt 2003).

The observed SEDs, f_λ , consist of *IUE* UV spectrophotometry (1165 – 3000 Å) and the optical V magnitudes, calibrated according to FM. As in FM, a weight is assigned to each *IUE* wavelength bin. This is a combination of the statistical errors in the data for that bin summed quadratically with an additional, systematic, uncertainty of 2.5% which accounts for residual low-frequency uncertainties in the data. We assign zero weight to the wavelength region 1195 – 1235 Å due to the presence of interstellar Ly α absorption. The V magnitude is assumed to be exact (however, see §4.1). We represent the stellar surface fluxes F_λ by *ATLAS9* model atmosphere fluxes, which are functions of four parameters: T_{eff} , $\log g$, [m/H], and v_{turb} . Because all of our program stars are lightly- or un-reddened we can utilize a predetermined form for the shape of the interstellar extinction curve and introduce very little error. All but the most deviant extinction curves differ by only a few magnitudes from the Galactic average curve. While this can result in huge effects for stars with significant extinction, for stars with color excesses of a few hundredths or less (as is the case here), the effect is minimal. Consequently, we adopt the $R(V) = 3.1$ extinction curve from Fitzpatrick (1999) to represent the shape of the extinction law. With these assumptions, we see that six parameters — T_{eff} , $\log g$, [m/H], v_{turb} , the attenuation factor $(R/d)^2$, and $E(B - V)$ — must be specified to completely define the SED of a lightly reddened star.

The data we utilize in the fitting process (*IUE* spectrophotometry and the V magnitude) strongly constrain three of the four parameters needed to specify the best-fitting *ATLAS9* models,

namely, T_{eff} , $[m/H]$, and v_{turb} , but are relatively insensitive to the fourth parameter, $\log g$. Consequently we require additional information to determine $\log g$. Normally, this could be achieved by comparing high-resolution spectroscopic observations of a Balmer line profile with Stark broadened model profiles. Unfortunately, we do not have such measurements at our disposal, and must look elsewhere. Our solution is to employ a combination of *Hipparcos*-based distances and stellar structure models, in conjunction with the SED data, to provide a very strong constraint on $\log g$ without appealing to hydrogen line data.

Our approach is to adopt the distances d implied by *Hipparcos* parallax measurements, which then allows us to determine the stellar radii R directly from the SED fitting procedure, rather than the ratio R/d (see Eq. 1). For main sequence stars, stellar structure models show that the surface gravity is uniquely identified by a star’s T_{eff} and R . This is demonstrated in Figure 1 using the Padova grid of structure models (Bressan et al. 1993) in the mass range of interest. Thus, by incorporating the distance constraint, we can fit the program star SEDs with five parameters (T_{eff} , $[m/H]$, v_{turb} , R , and $E(B-V)$) and then determine the surface gravity from stellar structure models *via* $\log g = \log g(T_{eff}, R)$. However, the surface gravity returned by the structure models is the “Newtonian” gravity,

$$g(Newton) \equiv G \frac{M}{R^2}, \quad (2)$$

which is not appropriate for describing the emergent flux of even moderately rotating stars, since the centrifugal force reduces the atmospheric pressure below that implied by $g(Newton)$. To compensate for this effect we make a first-order correction to $g(Newton)$ to derive the “spectroscopic” gravity,

$$g(Spec) \equiv g(Newton) - \frac{(v \sin i)^2}{R}. \quad (3)$$

This corrected value of the gravity is used to select the appropriate *ATLAS9* model and the whole process is iterated to achieve consistency. As a result of this procedure, we are able to derive well-defined estimates of all five fitting parameters, plus $\log g(Spec)$, from just the UV SED, V , $v \sin i$, and the *Hipparcos* distances.

To our knowledge, Herrero et al. (1992) were the first to formally correct spectroscopically-derived surface gravities for the effects of rotation — although such effects on gravity-sensitive spectral features have been recognized for some time (see, e.g., Gray & Garrison 1987). The form of the correction in Eq. 3 is based on the detailed discussion of Repolust et al. (2004). We emphasize that this a first-order correction to a complex effect and that more sophisticated approaches exist for interpreting the spectra of rapidly rotating stars (e.g., Collins & Truax 1995, Townsend et al. 2004). However, these results are highly model-dependent, are more appropriate for extremely rapidly rotating stars (which are not included our sample), require detailed line profiles for analysis (which we do not possess), and have never been fully verified. In contrast, the simplified adjustments we employ are easily applied and will be shown in § 7.2 to be entirely consistent with observations.

3. Data

3.1. The Observations

For this study, we restrict our attention to normal, non-supergiant, non-emission line, lightly-reddened ($E(B - V) \leq 0.03$) A and B stars with high quality low-resolution *IUE* spectra (Boggess et al. 1978) for both the short (SWP) and long (either LWP or LWR) wavelength ranges, high quality optical photometry, and *Hipparcos*-based distances with errors $\leq 10\%$ (Perryman et al. 1997). These criteria resulted in the sample of 45 stars listed in Table 1.

We use NEWSIPS *IUE* data (Nichols & Linsky 1996) obtained from the MAST archive at STScI. These data were corrected for residual systematic errors and placed onto the *HST*/FOS flux scale of Bohlin (1996) using the corrections and algorithms described by Massa & Fitzpatrick (2000; hereafter MF). Multiple spectra from each wavelength range (SWP or LWR and LWP) were combined using the NEWSIPS error arrays as weights. Small aperture data were scaled to the large aperture data and both trailed and point source data were included. Short and long wavelength data were joined at 1978 Å to form a complete spectrum covering the wavelength range $1150 \leq \lambda \leq 3000$ Å. Data longward of 3000 Å were ignored because they are typically of low quality and subject to residual systematic effects. The *IUE* data were resampled to match the wavelength binning of the *ATLAS9* model atmosphere calculations in the wavelength regions of interest.

Note that the MF corrections to the *IUE* NEWSIPS data are essential if precise absolute fluxes are required — as in the present study — since the systematic errors in these data are wavelength-dependent and approach 10% in some spectral regions. Although we have not performed a detailed examination of the European Space Agency’s version of *IUE* Final Archive (i.e., the INES database), spot examination of a number of INES spectra has shown that similar systematic problems affect these data. As with NEWSIPS, INES fluxes should be considered with caution, as the absolute calibration appears to be systematically in error and residual thermal and temporal affects may exist in the data.

Table 2 lists the Johnson *UBVRIJHK* and Strömgen *uvby β* photometry for the program stars and Table 3 lists the available Geneva color indices. All data in Tables 2 and 3 are mean values acquired via the Mermilliod et al. (1997) archive. Table 4 lists the *2MASS* *JHK* data along with their associated errors. These data were obtained from the *2MASS* All-Sky Point Source Catalog at the NASA/IPAC Infrared Science Archive.

3.2. The Models

The model data consist of stellar surface fluxes F_λ produced by the Kurucz (1991) *ATLAS9* model atmosphere code, in units of $\text{erg cm}^{-2} \text{sec}^{-1} \text{Å}^{-1}$. Since the resolution of the *IUE* (4.5 – 8 Å) is only slightly smaller than the size of the *ATLAS9* wavelength bins in the UV region (10 Å), the characteristics of binned *IUE* data do not exactly match those of *ATLAS9*, where the latter may

be thought of as resulting from the binning of very high resolution data. In essence, adjacent *IUE* bins are not independent of each other, while adjacent *ATLAS9* wavelength points are independent. To better match the *IUE* and *ATLAS9* data, we smooth the *ATLAS9* model fluxes in the *IUE* wavelength region by a Gaussian function with a FWHM of 6 Å. This slight smoothing simulates the effects of binning lower resolution data. FM have shown that these provide excellent fits to UV data.

4. Model Fitting

In this section, we present the results of the our fitting procedure and assess their observational errors.

The four panels of Figure 2 illustrate the results of the SED fitting procedure for the 45 program stars. The *IUE* (small circles) and *V*-band (large circles) data are shown, along with the best-fitting distance-attenuated and reddened *ATLAS9* models (histogram style curves). The stars are arbitrarily offset vertically for display purposes and are arranged in order of increasing T_{eff} , with the coolest at the bottom of the first panel and the hottest at the top of the last panel. As has been shown already by FM, Guinan et al. (1998, 2000), Ribas et al. (2000, 2002), and Fitzpatrick et al. (2002, 2003), the ability of the *ATLAS9* models to reproduce the UV SEDs is impressive.

Values of the fit parameters are listed in Table 5. Recall, from the discussion in § 2, that the first five parameters in the Table (T_{eff} , $[m/H]$, v_{turb} , R , and $E(B-V)$) are determined directly by the fit, while the sixth one ($\log g(Spec)$) is deduced utilizing the *Hipparcos* distances, $v \sin i$, and the Bressan et al. models. For completeness, we also list the value of the Newtonian gravity ($\log g(Newton)$) in the final column of the Table. To provide an overview of the properties of our calibration sample, we plot their temperatures and radii (plus the associated errors) on the theoretical HR Diagram shown in Figure 1.

4.1. The Uncertainties

The errors listed in Table 5 are 1- σ and incorporate a number of potential sources of uncertainty. The MPFIT least-squares routine provides estimates of the internal uncertainties for each of the parameters, based on the statistical errors in the input data (in this case, the *IUE* SEDs) and any covariant behavior of the parameters. However, additional uncertainty in the results arises from uncertainty in some of the assumptions in the analysis, which are not communicated to the fitting routine. These include random errors in the *V* magnitudes (which are assumed to be exact by the fitting algorithm) and in $v \sin i$; scaling errors in the *IUE* fluxes which translate to zero point offsets in their logarithms (see MF); uncertainties in the *Hipparcos* distances; and errors in the shape of the assumed extinction curve and its value of $R(V)$.

We incorporated these possible effects in our analysis using a Monte Carlo approach. The SED of each star was fit 100 times, with input parameters (i.e., V , IUE zero points, d , $k(\lambda - V)$, and $R(V)$) drawn randomly each time from parent samples generated by assuming Gaussian-like error distributions. These parent distributions were assumed to have the following properties:

1. All V magnitudes have $1-\sigma$ observational errors of ± 0.015 mag.
2. All $v \sin i$ values have $1-\sigma$ observational errors of $\pm 10\%$.
3. The logarithmic uncertainties in zero points of individual IUE spectra correspond to the scaling errors given in Table 5 of MF. In cases where multiple spectra were combined, the uncertainties are reduced accordingly. For example, a single LWR large aperture spectrum has a $1-\sigma$ zero-point uncertainty of $\pm 3.8\%$; when two such spectra are combined, the uncertainty reduces to $\pm 2.7\%$.
4. The $1-\sigma$ errors in the *Hipparcos* distances are those listed in Table 1.
5. The $1-\sigma$ uncertainty of $R(V)$ is ± 0.4 mag, and the corresponding changes in the shape of the extinction curve are calculated from the prescription given by Fitzpatrick (1999). This error in $R(V)$ produces a change in the normalized extinction at 1550 \AA of 0.69 mag, which slightly exceeds the RMS scatter found in randomly selected extinction curves for low density sight lines (see, Table II in Massa 1987).

For each star, the uncertainties listed in Table 5 were computed by quadratically combining the internal errors returned by MPFIT with the standard deviation observed for each output parameter within a set of 100 Monte Carlo SED fits.

Other potential sources of error include the adopted stellar interior models, which provide the $\log g$ values, and the *ATLAS9* stellar atmosphere models themselves. We tested the former by running the analysis utilizing the Geneva grid of stellar interior models (Schaller et al. 1992). This had virtually no effect on our results, since typical differences between the Geneva-based and Padova-based parameters are an order of magnitude (or more) smaller than the parameter uncertainties listed in Table 5. The issue of the precision of the *ATLAS9* model is beyond the scope of this paper. Here we can merely note that these models obviously yield extremely good fits to the observations (see Figure 1) and, in cases where substantial ancillary information exists (e.g., for eclipsing binary systems, see Fitzpatrick et al. 2003), they appear to yield precise and accurate values of the stellar properties.

A look at the results in Table 5 shows that the stellar properties are apparently very well-determined. Some faith in the results and the quoted uncertainties can be gained by considering the case for Vega (HD 172167), for which we find $T_{eff} = 9549 \pm 41$, $\log g = 3.96 \pm 0.01$, and $[\text{m}/\text{H}] = -0.51 \pm 0.07$. The error bars for our parameters are remarkably small, but the results are in excellent agreement with those from other investigators (see, e.g., Castelli & Kurucz 1994,

Qiu et al. 2001) and consistent to within the stated errors. In § 7, we provide additional evidence that our procedure has indeed yielded reasonable values for the stellar properties and that these are consistent with determinations from previous studies.

5. The Synthetic Photometry

This section describes the calculation and calibration of the synthetic photometry and presents the final results.

5.1. Calculation

Now that we have reliable SEDs with full wavelength coverage, all that is needed to compute the synthetic photometric magnitudes and indices is a set of sensitivity curves for the various filters. Table 6 lists the references for the sensitivity curves we have adopted. The uncalibrated synthetic photometry was calculated by convolving the model SED for each star with the appropriate filter sensitivity curve, scaled to unit area, and converting the result to magnitudes. The uncalibrated indices, such as $(B - V)_{syn}$, were computed by differencing the appropriate magnitudes. For the Johnson $B - V$ and $U - B$ indices, we followed the procedure of Buser & Kurucz (1978) and computed $(B - V)_{syn}$ with their B_3 and V filters and $(U - B)_{syn}$ with their U_3 and B_2 filters, using their naming convention.

Synthetic Strömgren β photometry requires some additional discussion. The β index — which measures the strength of the $H\beta$ line at 4861 Å and is very sensitive to surface gravity — is obtained by computing the difference between an intermediate-band magnitude and a narrow-band magnitude, both centered on $H\beta$. The width (FWHM) of the intermediate filter is typically in the range 90–150 Å while that of the narrow filter is 15–35 Å. We experimented with a variety of profiles for these filters, including those published by Crawford & Mander (1966) and actual profiles of filters currently in use at Kitt Peak Observatory. The very strong result of these experiments is that our final results are virtually independent of which filter set we choose for the synthetic photometry since, as in the case of real photometry, a transformation relation maps the synthetic photometry onto the standard system. The different filter combinations do, of course, lead to different transformations and we based our choice of filter on the shape of the relation. Our ultimate choices were Gaussian-shaped filters with FWHM values of 90 Å and 15 Å, which are reminiscent of the filters used by Crawford (1958) in the early establishment of the β system and which allow a simple linear transformation to the standard system. These filters are shown in Figure 3, compared to a synthetic $H\beta$ profile corresponding to a main sequence star with $T_{eff} = 15000$ K.

Because of the narrowness of the β filters, the synthetic photometry cannot be performed directly on the low-resolution *ATLAS9* SEDs, which are binned at 20 Å intervals near $H\beta$. Instead, we first computed high-resolution synthetic spectra for each *ATLAS9* model — sampled at 0.1 Å over a 400 Å interval centered on $H\beta$ — utilizing the *SYNSPEC* spectral synthesis program (Hubeny & Lanz 2000). We then calculated the synthetic photometry using these spectra and with the filter profiles scaled to peak values of unity. The $H\beta$ line seen in Figure 3 is from this set of calculations.

5.2. Calibration

The last step in the calibration of the synthetic photometry is determining the functional relationship between the synthetic magnitudes and indices and the observed photometry for the 45 program stars. Figures 4 through 7 show these transformation relationships for the Johnson, Strömgren, and Geneva filters. In each panel of the figures, the solid line has a slope of unity and shows the mean offset between the observed and synthetic values. In cases where such a simple offset is deemed insufficient to describe the relationship between observed and synthetic values, the adopted transformation is shown by a dashed line. The standard deviations (σ), or “scatter,” of the observed indices around the adopted transformation lines are indicated in the lower right of each panel of Figures 4–7.

For $B - V$, m_1 , $(V - B)_{Geneva}$, $(G - B)_{Geneva}$, J , H , and K , a simple offset provides the best transformation relationship, with little or no improvement from the use of higher order terms or color terms. All the other colors and indices required a linear term, indicated in their respective panels by the dashed lines.

Note that the β index is well represented by a linear transformation, although the dynamic range of the synthetic index is somewhat larger than for the standard system (i.e., the slope of the transformation is less than 1.0). We found that we could steepen the relation to better match the standard system by, for example, widening the adopted 15 Å filter. However, this always resulted in significant curvature in the transformation *with no improvement in the scatter of the observed data about the transformation curve* and we opted for the simpler transformation. As will be shown below, the observed scatter is consistent with the known sources of random error.

Figure 8 shows the differences between the observed and synthetic *2MASS* magnitudes plotted against the observed values. The error bars are for the observed photometry, as listed in Table 4. For each filter there are clearly two distinct groups of data points, one well-determined and one poorly-determined. This arises because the images of our brightest stars are highly saturated in *2MASS* observations and the derived magnitudes are highly uncertain, with $1-\sigma$ errors of ~ 0.2 – 0.3 mag. For the fainter stars, the errors are a factor of 10 smaller. The horizontal dashed lines in Figure 8 show the simple mean offset between the observed and synthetic magnitudes, based only on the well-determined observations. No higher order terms are required in the transformation and it is gratifying that there appears to be no systematic difference between the results for the brightest stars and the rest of the *2MASS* sample. The standard deviations of the observed data about the mean transformation lines are indicated in each panel of Figure 8, computed only from the data with errors less than 0.1 mag.

The detailed level of agreement between the observed and synthetic photometric indices, i.e., the “scatter” about the mean transformation lines in Figures 4–8, provides some insight into the accuracy of our procedure. If the calibrations are correct, then the scatter of the observed data about the transformation relations should result from the simple quadratic sum of the observational errors and the random errors in the synthetic photometry. Thus, comparing the observational errors,

synthetic photometry errors, and observed transformation scatter allows us to examine whether the error estimates for the stellar properties are reasonable (see § 4.1) and whether some additional sources of error are present in the procedure.

The data for these comparisons are summarized in Table 7. The second column lists the transformation scatter for each index (as shown in Figures 4-8). The third column gives the expected errors in the synthetic indices. These arise from the uncertainties in the SED fitting procedure (e.g., the uncertainty in the best-fitting values of T_{eff}) and were estimated for each star by performing synthetic photometry on each of the 100 Monte Carlo fits described in the previous section. This resulted in standard deviations for each synthetic photometric index in each star. We then computed the RMS mean of these standard deviations for each index, averaging over all the stars. This provides an estimate of the characteristic uncertainty of the synthetic photometry for our program stars. Finally, the quadratic difference between the transformation scatter and the synthetic photometry error provides an estimate of the actual observational errors in the data, in the absence of any other significant source of random error. This estimate is given on the fourth column of Table 7.

Examination of the results in Table 7 shows that the observational uncertainties implied by the scatter seen in our transformation relations are completely consistent with expected uncertainties, which are listed in the final column of the table. Among the optical Johnson, Strömgren, and Geneva indices, only the Geneva $U - B$ color shows a significantly larger scatter than expected. However, we suspect that the “expected” value is somewhat optimistic given the inherent difficulties with atmospheric extinction corrections for the broadband U filter. This effect leads to the larger scatter (both observed and expected) for the Johnson $U - B$ color and probably affects the Geneva $U - B$ color in a similar way. We are not aware of analyses of the expected uncertainties in Johnson $V - R$ and $R - I$ photometry. However, given the great breadth of the filters, and the wide range in the properties of the filters actually in use — both of which compromise the transformability of the photometry — the “predicted” scatter of 0.02–0.03 mag seems reasonable. The small number of program stars for which Johnson JHK data are available make the derived estimates of the observational scatter uncertain, but the results are clearly consistent with errors of 0.01–0.02 mag, which are also reasonable.

For the *2MASS* data, we can compare the predicted observational errors directly with the errors provided with the data. These two sets of results are listed in Table 7, utilizing only the “well-determined” observations, as described above. For J_{2M} and K_{2M} the results are consistent, but the calibration scatter for H_{2M} is significantly larger than can be accounted for by the quoted observational errors and our expected synthetic photometry errors. Since the H_{2M} band straddles the head of the hydrogen Brackett series it seemed possible that inadequacies in the *ATLAS9* SEDs could produce larger random errors than we computed if, for example, the strengths of the higher order Brackett lines were more or less temperature-sensitive than predicted by the models. However, we find no evidence in our results for such an effect. The H_{2M} transformation scatter for the cooler stars, where the Brackett lines are stronger, is actually slightly smaller than for the

hotter stars, where the lines are intrinsically weaker. We tentatively conclude that the observational errors for H_{2M} , which are already larger than for J_{2M} and K_{2M} , may be underestimated, perhaps due to larger-than-expected variations in atmospheric transmission in this band. Note that the transformation scatter for the Johnson H is also larger than for the nearby J and K bands, also indicting larger observational uncertainties.

Recently, Cohen (2003) published a detailed calibration for the *2MASS* filters, based on a sample of 33 A0-through-M0 stars. Although the dynamic range of this sample greatly exceeds ours — in terms of both magnitude and color — the results are quite compatible. In the simplest terms, J , H , and K magnitudes derived using our calibration can be transformed to Cohen’s system by adding 0.024, 0.007, and 0.023 mag, respectively for the three filters. This consistency is a testament to the uniformity of the *2MASS* database and the accuracy of the *2MASS* filter sensitivity curves.

Our overall conclusion from considering the results in Table 7 and Figures 4–8 is that the synthetic photometry based on the *ATLAS9* models is well-behaved and readily transformed to the standard photometric systems. Further, the consistency between the expected scatter in the calibration relations and that actually measured indicates that our error analysis has provided reasonable estimates of the uncertainties in the parameters describing the models and thus, the stellar properties.

6. Final Results

The captions to Figures 4–8 contain the actual transformation relations for all the photometric indices; however, these are not particularly useful to the reader since they depend in detail on exactly how we computed the synthetic values. Of more use are the actual calibrated synthetic indices themselves. In Tables 8, 9, 10, and 11, we present the calibrated photometry for all the models in our *ATLAS9* grid for the Johnson, Strömgren, Geneva, and *2MASS* systems, respectively. As described by FM, this grid consists of models with T_{eff} between 9000 K and 50000 K and $\log g$ from 5.0 down to the Eddington limit for five different values of the metal abundance ($[m/H] = -1.5, -1.0, -0.5, 0.0, 0.5$) and five different microturbulence velocities ($v_{turb} = 0, 1, 2, 4, 8 \text{ km s}^{-1}$). There are a total of 8847 models in the grid. Each of the tables is subdivided into 25 parts (e.g., “8a”, “8b”, etc.), with each part containing the photometric indices for one combination of $[m/H]$ and v_{turb} . In the interest of saving space, we show here only a small portion of Tables 8a, 9a, 10a, and 11a. The complete versions of the tables are available in the electronic edition of the Journal.

7. Discussion

Our goal has been to derive a calibration of synthetic photometry from the *ATLAS9* model grid which will enable us to infer the physical properties of a star and its line-of-sight extinction

from observations of its UV continuum and optical photometry. To determine the calibration, we constrained the models by demanding that the derived physical properties be consistent with a set of conditions imposed by a combination of *Hipparcos* data and stellar structure models.

Now that we have a calibration of the optical and NIR photometry, three issues arise:

1. *Are the fits and the derived physical properties reasonable?*
2. *How well can the stellar properties be determined?*
3. *How is the best fit determined when *Hipparcos* data are unavailable?*

To answer the first question, we compare our derived stellar properties to previous, accepted values, as assigned to their spectral types or derived from their *uvby β* photometry. To answer the second question, we must evaluate the influence of both measurement and systematic errors on the derived parameters. The third question amounts applying the calibration to the synthetic photometry and then re-deriving the physical properties from the UV and optical photometry alone. This process also forces us to address the question of how to assign weights to the UV and optical photometry.

7.1. Comparison to previous results

It is important to verify our fitting procedure by comparing the physical properties we derive with those obtained by previous investigators. We begin by examining the relationship between T_{eff} and MK spectral type. Figure 9, displays the derived temperatures versus the spectral types for the program stars (filled circles). There is only one disparate point, and that is for the hottest star in our sample, ζ Cen (HD 121263), which is classified as B2.5 IV by Hiltner, Garrison, & Schild (1969). However, the low resolution UV spectrum of this star is nearly identical to that of the unreddened B1 V star HD 31726 (too distant to be in the current sample), and differs significantly from other B2 stars in our sample. Furthermore, this star has been previously classified as B1 V by Woolley, Gascoigne, & de Vaucouleurs (1954) and its *uvby β* photometry (see below) is also consistent with a B1 V star. Thus, we suspect a classification error in this case. Figure 9 also shows a number of spectral type vs. T_{eff} calibrations taken from the literature (and identified in the figure). It is clear that our results are quite consistent with past evaluations.

A commonly used method for calculating the temperatures and surface gravities of A and B stars is to derive them from Strömberg *uvby β* photometry. Because the photometry does not provide adequate information to determine $[m/H]$ or v_{turb} for B stars, these are typically either fixed or derived from a fine analysis of the spectrum. Napiwotzki (2004) provides an updated version of the widely used Moon & Dworetzky (1985) synthetic photometry calibration, which is also based on *ATLAS9* models. We have used this program to calculate T_{eff} and $\log g$ from *uvby β* photometry for each program star. We plot these photometry-based properties against ours in Figures 10. It is immediately apparent that the agreement is quite good, with very small

systematic differences or scatter. The mean differences (ours minus $uvby\beta$) and their RMS scatters are: $\Delta \log T_{\text{eff}} = 0.000 \pm 0.009$ and $\Delta \log g = 0.03 \pm 0.13$, indicating that the small offsets are well within the scatter.

It should be emphasized that the two T_{eff} and $\log g$ determinations presented in Figures 10 *have no input data in common*. The properties we derive are based on absolutely calibrated UV spectrophotometry, V band fluxes, $v \sin i$ values, and *Hipparcos* distances, while the comparison values are based on $uvby\beta$ photometry alone — although both are ultimately tied to the *ATLAS9* models. This comparison demonstrates that both approaches are measuring the same quantities and gives us confidence in our approach. It also demonstrates that the calibration of the synthetic $uvby\beta$ photometry that we derive will be nearly identical to the one used by NSW. In addition, it shows minimal systematic differences between the two methods of calculating physical properties.

We can also examine how well our derived abundances agree with previous determinations. As FM point out, the abundances we measure result from features in the UV continua, and these are primarily due to iron group elements. One source of iron-group abundances for bright, normal B stars is the Smith & Dworetzky (1993) fine-analysis of high-resolution *IUE* spectra. Although we have only 5 stars in common (HD 38899, HD 147394, HD 172167, HD 193432 and HD 215573), it is encouraging that, of these, the ones with the largest and smallest Fe abundances found by Smith & Dworetzky (HD 147394 and HD 172167, respectively) also have the lowest and largest $[\text{m}/\text{H}]$ and that the range is similar, 0.70 dex for Fe and 0.75 dex for $[\text{m}/\text{H}]$. Recently, Hempel & Holweger (2003) determined Fe abundances for two of our program stars, HD 21790 and HD 218045, from a NLTE analysis of optical iron lines. They found $[\text{Fe}/\text{H}]$ values of -0.43 and -0.10, respectively, for a difference of -0.33. For the same stars, we find $[\text{m}/\text{H}]$ of -0.64 and -0.02, for a difference of -0.62. Again, the ordering is correct, and the magnitude of the difference agrees reasonable well, considering the very different methods used.

In addition to abundances, Smith & Dworetzky also provide v_{turb} measurements, but there is no relation between their values and ours. This is not surprising, given the different methods used to arrive at this parameter and the fact that range observed in our current sample barely exceeds the internal errors (see Table 5).

Finally, angular diameter measurements by Hanbury Brown et al. (1974) are available for three of our program stars, γ Gem, α Leo and α Lyr. They obtained limb darkened angular diameters of 1.39 ± 0.09 , 1.37 ± 0.06 and 3.24 ± 0.07 mas, respectively, for these stars. Using our derived radii from Table 5 and the *Hipparcos* distances from Table 1, we determine angular diameters of 1.43 ± 0.02 , 1.39 ± 0.02 and 3.28 ± 0.04 mas for the same stars, where our major source of error is the uncertainties in the *Hipparcos* distances. We see that all of the available measurements are consistent to less than one σ .

The comparisons presented in this section show that our calibration (which relies only on UV spectrophotometry, calibrated V photometry and *Hipparcos* distances), yields physical properties that agree with those found by commonly accepted methods.

7.2. Errors in the derived parameters

While the formal fitting errors in the derived stellar properties listed in Table 5 are quite small, we recognize that the actual errors in the physical properties may be considerably larger, due to systematic effects. To properly evaluate such effects, we need a determination of the stellar properties based on an independent data set. The T_{eff} and $\log g$ values determined from $uvby\beta$ photometry form such a set. As noted earlier, the $uvby\beta$ and *Hipparcos*-constrained data sets are completely independent of one another, making their comparison free of bias. To perform the comparison, we simply examine the standard deviation of the differences between the parameters derived from the two data sets and then subtract, quadratically, the expected error for the $uvby\beta$ determinations. The result is an independent estimate of the errors in the *Hipparcos*-constrained properties.

To proceed, we must first determine the expected errors in the T_{eff} and $\log g$ values derived from the $uvby\beta$ data. This is done by performing a Monte Carlo simulation of the sort described in § 4.1. Using the values listed in Table 7 for the errors in the $uvby\beta$ indices, we ran 100 trials for each star with the random errors added to the photometric indices and then calculated new values of T_{eff} and $\log g$ with the Napiwotzki program to obtain the variances for each star. We then calculated the RMS error expected from random uncertainties in the $uvby\beta$ photometry. The results are $\sigma(\log T_{eff})_{uvby\beta} = 0.0072$ and $\sigma(\log g)_{uvby\beta} = 0.127$.

We now have the data required to evaluate our errors, and we begin with T_{eff} . The standard deviation of the differences between the *Hipparcos* and $uvby\beta$ determinations is $\sigma(\Delta \log T_{eff}) = 0.0090$ and, thus, the predicted error for the *Hipparcos*-based temperatures is $\sqrt{0.0090^2 - 0.0072^2} = 0.0054$. The RMS mean of the formal errors listed in Table 5 is 0.0048 and so we see that the derived error is only slightly larger than the internal error (1.3% in T_{eff} as opposed to 1.1%). Thus, we suspect that the T_{eff} are relatively free of systematics and that the formal fitting errors are close to the actual errors, and somewhat smaller than the errors in the T_{eff} determined from $uvby\beta$ photometry (1.3% vs. 1.7%).

Turning now to the surface gravity, we find that the standard deviation of the differences of all the data in Figure 10 is $\sigma(\Delta \log g) = 0.132$, which implies an expected error in our *Hipparcos*-based results of $\sqrt{0.132^2 - 0.127^2} = 0.036$. This is actually smaller than the RMS of the formal errors for $\log g(Spec)$ in Table 5, which is 0.063. As with T_{eff} , the comparison suggests that our determinations of $\log g(Spec)$ are free of strong systematics and that the formal fitting errors are consistent with the actual errors, and considerably smaller than the errors in the $\log g$ determined from $uvby\beta$ photometry.

The consistency between our $\log g(Spec)$ values and those based on $uvby\beta$ data provides an important validation for our correction of the Newtonian gravities for the effects of rotation (see Eq. 3 in §2). The impact that this correction has had on our results is illustrated in Figure 11 where we plot the residuals between the $uvby\beta$ -based gravities and our values for $\log g(Newton)$ and $\log g(Spec)$, both as a function of $v \sin i$. The top panel shows that, had we *not* corrected the

Newtonian gravities for the effects of rotation, the overall scatter between our results and the $uvby\beta$ -based results would have increased (from ± 0.132 to ± 0.159) and a strong systematic effect would have been introduced into our results, whose roots can be traced all the way down to $v \sin i \simeq 200$ km/sec. In our sample, the star with the largest positive residual (i.e., $\log g - \log g(uvby\beta)$) is HD 225132. (This star, located at $v \sin i = 190$ km s⁻¹, lies outside the bounds of the top panel of Figure 11 but stands out clearly in the lower panel.) If this discrepancy were a simple rotational effect, it would require a $v \sin i$ value of greater than 350 km/sec for our first-order correction to reconcile $\log g(Spec)$ with $\log g(uvby\beta)$. However, the observed value of 190 km/sec seems well-determined and is clearly too slow to explain the discrepancy in a simple way. It could be that this star is an extremely rapidly rotating object which is viewed close to pole on, and is sufficiently distorted to make our correction invalid. Such a situation might be revealed through detailed study of its absorption line profiles. This star deserves further attention.

Our approach should not be confused with the direct application of models for rotating stars as applied by Wenske & Schönberner (1993). They derived T_{eff} and $\log g$ for stars from $uvby\beta$ photometry and then used Collins et al. (1991) models and observed $v \sin i$ measurements to “correct” both T_{eff} and $\log g$ for the most probable effects of rotation and to infer the T_{eff} and $\log g$ of an equivalent *non-rotating* star of the same mass. Our approach is more direct. To begin, recall that we discarded Be stars from our sample, so we have probably eliminated stars rotating within 75% of their critical velocity (see Massa 1975). We then obtain a T_{eff} and $E(B - V)$ by fitting the observed UV SED and V photometry to a model, assuming $\log g = 4.0$ for the initial iteration. With this estimate for T_{eff} and the *Hipparcos* distance, we calculate the stellar radius. We then determine the mass of the star (and hence its Newtonian gravity) from its position on a theoretical HRD expressed in terms of T_{eff} and R/R_{\odot} . This $\log g$ is used to redetermine the T_{eff} and $E(B - V)$. We then derive a new mass and $\log g$, iterating to consistency. Throughout the iteration process, T_{eff} changes by typically less than 50 K. The result of our fits are an actual T_{eff} (not the temperature of an equivalent, non-rotating star of the same mass) which must agree with the integrated surface flux of the star. Similarly, the $\log g$ we derive is a Newtonian surface gravity, determined directly from the stellar mass and radius. However, the $\log g$ which corresponds to the β photometry is a measure of the mean atmospheric pressure, and not the Newtonian gravity. Consequently, we must adjust the Newtonian surface gravity to that expected for a rotating star – otherwise the predicted β index will not agree with the observed value. Our procedure is verified by the positions of the most rapidly rotating stars in the photometric transformation diagrams (Figs. 4–7). Their points are circled in these diagrams and are generally unremarkable, particularly in the β diagram, suggesting that the Repolust et al. (2004) corrections are reasonable. Note, however, that a few of the rapidly rotating stars are outliers in the $c1$ and the $(U - B)_{Geneva}$ diagrams, even though their corrected β indices (which are most sensitive to surface gravity) are normal. This may indicate that the SEDs of the most rapidly rotating stars are affected by rotation in other ways. One possible cause is the expected non-uniform temperature distribution over the surface of a rapidly rotating star, an effect not included in the Repolust et al. corrections. It would take a more focused and detailed investigation to isolate such effects

Notice also that there are several stars with large negative residuals in Figure 11, particularly HD 153808, HD 188665, and HD 199081, for which the residuals are < -0.2 dex in both panels of the figure. Two of these, (HD 153808 and HD 199081, shown with open symbols in Fig. 11) are double-lined spectroscopic binaries (“SB2s”). Since our analysis has treated these systems as single objects, the combination of their observed brightness and the distance constraint imposed by the *Hipparcos* data yielded a radius larger than either member of the binary, resulting in an underestimate of the surface gravity (see Figure 1). In the case of two identical stars, the result is a simple factor-of-2 error, with the *Hipparcos*-based gravities being ~ 0.3 dex too small, comparable to the observed discrepancy for HD 153808 and HD 199081. The third star, HD 188665, has a similar discrepancy, although it is not known to be a binary. The data in Figure 11 might be evidence for the binarity of this object. Note that this binary-induced error in $\log g$ is peculiar to our *Hipparcos*-based approach. Spectroscopic determinations are immune to the effect and will yield a value of $\log g$ which is a weighted mean of the two binary members, depending on their relative contributions to the light.

The total errors affecting $[m/H]$ and v_{turb} are more difficult to assess. It is clear from the previous section that the our fitting procedure identifies specific stars which are known to have extreme abundance anomalies. However, we lack the large, uniformly-analyzed sample of independently determined abundances which is needed to obtain a quantitative estimate of the total error affecting our metallicity measurements. As for v_{turb} , the question of errors is nearly irrelevant for the current sample. By confining our sample to nearby, low luminosity stars, the maximum value of v_{turb} for any star in our sample is only 2.1 km s^{-1} , and typical errors are $0.5 - 1.0 \text{ km s}^{-1}$. As a result, it is problematic to identify any systematic dependencies involving v_{turb} from the current sample. In the future, we may be able to assess the accuracy of $[m/H]$ and v_{turb} indirectly by, for example, examining the scatter of $[m/H]$ within a cluster, or the dependency of v_{turb} upon luminosity in a larger sample of stars. However, until such samples are available, we must consider the values listed in Table 5 as lower limits to the actual errors for these parameters.

In summary, we see that the our estimates for T_{eff} are free of systematics and have random errors that are somewhat smaller than the errors affecting temperatures derived from optical photometry alone. We have also seen that our *Hipparcos*-based approach has yielded accurate values of $\log g(Spec)$ with small and well-determined random errors. On the other hand, our analysis has highlighted an important systematic effect which may affect many analyses. Namely, that spectroscopically-based surface gravity determinations (e.g., from β photometry or from line profile analysis) may systematically underestimate the actual Newtonian gravity (i.e., GM/R^2) of a star, in the presence of even moderate rotation (i.e., $v \sin i > 200 \text{ km/sec}$). The most obvious area of concern is when spectroscopically-based gravities are used to place stars in theoretical HR Diagrams for comparison with stellar structure and evolution models, as discussed by Herrero et al. (1992). Knowledge of a star’s rotation would appear to be an essential piece of information for such studies.

7.3. Applying the calibration

In our own future analyses, the most common application of the calibrated synthetic photometry will be to model the SEDs of stars (both reddened and unreddened) by combining *IUE* UV spectrophotometry and an ensemble of available ground-based photometry. This combination provides powerful constraints on SED models, including both the intrinsic properties of the stars and the effects of interstellar extinction. In particular, the UV data provide exclusive information on v_{turb} , $[m/H]$, and the shape of the UV extinction law. The combined UV and optical/near-IR photometry present a very long wavelength baseline for the determination of T_{eff} . In addition, the optical and near-IR continuum data provide access to the Balmer Jump (a useful temperature and gravity diagnostic) and the important extinction parameters $E(B - V)$ and $A(V)$. Finally, β photometry is extremely sensitive to luminosity (Crawford 1958) or, equivalently, $\log g$. When a full suite of photometry is available, there is considerable redundancy. However, this redundancy reduces the effects of random errors in the individual measurements, and allows the identification of the occasional pathological data point.

When fitting a UV/optical/near-IR SED, we must decide how to weight the various data sets in the least-squares procedure. Clearly, if we simply use the observational errors, this would assign most of the weight to the UV, since it contains so many points. However, this is undesirable since the stellar and interstellar information is spread throughout the spectrum. Given this distribution of information, we decided to divide the fitting weights into three groups: one for the UV, one for the optical/near-IR continuum photometry, and one for the β photometry. After considerable experimentation, we adopted the simple procedure of assigning identical total weight to each group, and distributing the weights within a group according to the observational errors. This balance between the UV and the optical/near-IR is intuitively appealing, although the great weight given to a single photometric index, β , merits comment. We have adopted this procedure essentially to insure that the $\log g$ results of the fitting procedure — in the absence of a *Hipparcos* constraint which would otherwise select the appropriate gravity — be consistent with photometric results based on *uvby* β photometry, as discussed in the previous section.

To test the above approach, we applied the SED fitting technique to our 45-star sample and calculated errors via the Monte Carlo approach described in § 4.1, except that random realizations of the input photometric indices — based on their expected errors (see Table 7) — were also included. Next, we examined the differences between the *Hipparcos*-based and the new SED-based properties for T_{eff} , $[m/H]$, and v_{turb} , and between the *uvby* β -based and SED-based values for $\log g$. The RMS errors for these samples are $\sigma(\log T_{eff})_{hip} = 0.0048$, $\sigma([m/H])_{hip} = 0.138$, $\sigma(v_{turb})_{hip} = 0.644$, and $\sigma(\log T_{eff})_{SED} = 0.0033$, $\sigma([m/H])_{SED} = 0.111$, $\sigma(v_{turb})_{SED} = 0.797$, for the *Hipparcos* and SED based parameters respectively. The means and standard deviations of the differences between these properties are: $\Delta \log T_{eff} = -0.0013 \pm 0.0066$; $\Delta [m/H] = 0.019 \pm 0.132$; and $\Delta v_{turb} = -0.14 \pm 0.579$. For totally uncorrelated data, we would expect $\sigma(\Delta x) \simeq \sqrt{\sigma(x)_{hip}^2 + \sigma(x)_{SED}^2}$, while for completely correlated data, we expect $\sigma(\Delta x) \simeq 0$. For $[m/H]$ and v_{turb} , we find $\sigma(\Delta x) \simeq \sigma(x)_{hip} \simeq \sigma(x)_{SED}$,

implying that errors in these properties are strongly correlated. This is because these measurements depend almost exclusively on the UV SED (which is common to both data sets), and only weakly on the optical/near-IR data. For T_{eff} , we find that $\sigma(\Delta T_{eff})$ and $\sqrt{0.0048^2 + 0.0033^2} = 0.0058$, are comparable, suggesting that the T_{eff} values derived from the SEDs are strongly influenced by the optical/near-IR data. This is reasonable, since T_{eff} determinations are sensitive to the total wavelength baseline, and the SED values incorporate significant, uncorrelated data. Finally, we compared our SED-based surface gravities with the $uvby\beta$ -based values discussed in §7.2, since our goal is to make the two as consistent as possible. The results are: $\sigma(\log g)_{uvby\beta} = 0.117$, $\sigma(\log g)_{SED} = 0.106$, and $\Delta(\log g) = \log g_{SED} - \log g_{uvby\beta} = -0.017 \pm 0.061$ for the entire sample. This time, we find that the standard deviation in $\Delta(\log g)$ is much less than *either* $\sigma(\log g)_{SED}$ or $\sigma(\log g)_{uvby\beta}$, indicating a very high degree of correlation, as desired.

Thus, although the details of the fitting procedure are somewhat subjective, the results of this section demonstrate that we are able to achieve excellent agreement between the physical properties determined from the SED fitting (without the *Hipparcos* constraint) and the other techniques.

8. Summary and Future Directions

To summarize, we have derived a calibration of synthetic optical and NIR photometry from *ATLAS9* model atmospheres which is based on *IUE* UV spectrophotometry, *V* band fluxes and *Hipparcos* distances. The result is a set of calibrated synthetic photometry which is consistent from the UV to NIR. We have also shown that spectroscopically-based determinations of $\log g$ — such as derived from β photometry — for stars with $v \sin i \geq 200 \text{ km s}^{-1}$ are systematically lower than the true Newtonian gravities, GM/R^2 .

The ability to predict the intrinsic UV continuum of a star and to derive $[m/H]$ and v_{turb} will allow us to pursue several important applications. Some of these are:

1. **Large study of unreddened stars:** We have identified approximately 150 lightly reddened early A and B stars with high quality *IUE* data and optical photometry. This sample will be used to search for systematic effects among the derived physical properties. It will also be used to extend the present results to hotter stars, in order to better define the range of applicability of the our approach. In particular, the availability of a large sample of stars, with uniformly determined v_{turb} values, will enable us to examine the dependence this poorly understood parameter on other factors, such as T_{eff} , $\log g$, mass loss, $v \sin i$, etc.
2. **UV reddening:** Because the models provide a precise intrinsic stellar continuum, we can use our approach to determine the UV extinction affecting a star without appealing to the subjective process of selecting an unreddened spectral match. FM provided an example of an extinction curve derived by fitting a model to a moderately reddened star. More recently, Massa & Fitzpatrick (2004) demonstrated how this same approach can be used to derive

extinction curves from lightly reddened stars, enabling studies of local and Galactic halo dust.

3. **Open Clusters:** Fitzpatrick & Massa (1990) list 5 open clusters which contain several main sequence B stars and additional examples exist in the *IUE* archives. By fitting the B star members of open clusters, we will be able to: 1) determine the small scale uniformity of UV extinction much more precisely than previously possible, 2) derive $R(V)$ values, needed to obtain accurate unreddened magnitudes, 3) calculate precise temperatures and gravities, needed to construct theoretical HRDs, 4) derive metallicities, to study the uniformity of cluster composition, and 5) determine the unreddened continua of cluster stars with unknown continua (Massa et al. 1985).
4. **The distribution of metallicity:** The ability to determine accurate metallicities for virtually every main sequence B and early-A star observed by *IUE* will enable us to search for systematic patterns in the distribution of metallicity in cluster and field A and B stars.
5. **Far UV fluxes:** Using the intrinsic fluxes determined from *IUE* and optical photometry, we will be able to test the validity of the models in the FUV by comparing them to *FUSE* observations of lightly reddened and reddened B stars. This will be a challenging test of the models, since the FUV is rich in spectral lines. If the comparisons for lightly reddened stars are favorable, we will have the confidence needed to derive accurate FUV extinction curves for reddened B stars.

Clearly, the approach outlined in this paper opens the door for several types of fundamental research on both stars and interstellar dust.

We are very grateful for a detailed and thoughtful review of this paper by the referee, Dr. R. Napiwotzki. E.F. acknowledges support from NASA grant NAG5-12137 and thanks Bernard Nicolet for making the Geneva photometry passbands available. D.M. acknowledges support from NASA grant NNG04EC01P. Some of the data presented in this paper were obtained from the Multimission Archive at the Space Telescope Science Institute (MAST). STScI is operated by the Association of Universities for Research in Astronomy, Inc., under NASA contract NAS5-26555. Support for MAST for non-HST data is provided by the NASA Office of Space Science via grant NAG5-7584 and by other grants and contracts. This publication also makes use of data products from the Two Micron All Sky Survey, which is a joint project of the University of Massachusetts and the Infrared Processing and Analysis Center/California Institute of Technology, funded by the National Aeronautics and Space Administration and the National Science Foundation.

REFERENCES

Balona, L. A. 1984, MNRAS, 211, 937

- Beeckmans, F. 1977, *A&A*, 60, 1
- Bessel, M.S., & Brett, J.M. 1988, *PASP*, 100, 1134
- Bessel, M.S., Castelli, F., & Plez, B. 1998, *A&A*, 333, 231
- Bogges, A., Carr, F. A, Evans, D. C., Fischel, D., Freeman, H. R., Fuechsel, C. F., KlingleSmith, D. A., Krueger, V. L., Longanecker, G. W., & Moore, J. V. 1978, *Nature*, 275, 372
- Bohlin, R. C. 1996, *AJ*, 111, 1743
- Böhm-Vitense, E. 1981, *ARA&A*, 19, 295
- Bressan, A., Fagotto, F., Bertelli, G, & Chiosi, C. 1993, *A&AS*, 100, 647
- Buser, R. & Kurucz, R. L. 1978, *A&A*, 70, 555
- Carpenter, J.M. 2001, *AJ*, 121, 2851
- Castelli, F. & Kurucz, R.L. 1994, *A&A*, 281, 817
- Code, A. D., Davis, J., Bless, R. C., & Hanbury Brown, R. 1976, *ApJ*, 203, 417
- Cohen, M., Wheaton, W.A., & Megeath, S.T. 2003, *AJ*, 126, 1090.
- Collins, G.W., & Truax, R.J. 1995, *ApJ*, 439, 860
- Collins, G.W., Truax, R.J. & Cranmer, S.R. 1991, *ApJS*, 77, 541
- Cowley, A., Cowley, C., Jaschek, M., & Jaschek, C. 1969, *AJ*, 74, 375
- Crawford, D.L. 1958, *ApJ*, 128, 185
- Crawford, D.L. & Mander, J. 1966, *AJ*, 71, 114
- Cutri, R. M., et al. 2000, Explanatory Supplement to the 2MASS Second Incremental Data Release, <http://www.ipac.caltech.edu/2mass/releases/second/doc/explsup.html>
- FitzGerald, M.P. 1973, *A&AS*, 9, 297
- Fitzpatrick, E. L. 1999 *PASP*, 111, 63
- Fitzpatrick, E. L. & Massa, D. 1999, *ApJ*, 525, 1011
- Fitzpatrick, E. L., Ribas, I., Guinan, E. F., DeWarf, L. E., Maloney, F. P., & Massa, D. 2002, *ApJ*, 564, 260
- Fitzpatrick, E. L., Ribas, I., Guinan, E. F., Maloney, F. P., & Claret, A. 2003, *ApJ*, 587, 685
- Flower, P.J. 1977, *A&A*, 54 31

- Garrison, R. F. & Gray, R. O. 1994, *AJ*, 107, 1556
- Glebocki, R., & Stawikowski, A. 2000, *Acta Astronomica*, 50, 509
- Gray, R. O. & Garrison, R. F. 1987, *ApJ*, 65, 581
- Guinan, E. F., Fitzpatrick, E. L., DeWarf, L. E., Maloney, F. P., Maurone, P. A., Ribas, I., Pritchard, J. D., Bradstreet, D. H. & Giménez, Á. 1998, *ApJ*, 509, 21
- Guinan, E. F., Ribas, I., Fitzpatrick, E. L., Gimenez, Á., Jordi, C., McCook, G. P. & Popper, D. M. 2000, *ApJ*, 544, 409
- Hempel, M., & Holweger, H. 2003, *A&A*, 408, 1065
- Herrero, A., Kudritzki, R. P., Vilchez, J. M., Kunze, D., Butler, K., & Haser, S. 1992, *A&A*, 261, 209
- Hiltner, W. A., Garrison, R. F., & Schild, R. E. 1969, *ApJ*, 157, 313
- Hoffleit, D. (with the collaboration of Jaschek, C.) 1982, *The Bright Star Catalogue*, 4th revised edition (New Haven: Yale University Observatory).
- Hubeny, I., & Lanz, T. 2000, <http://tlusty.gsfc.nasa.gov/Synspec43/synspec.html>
- Humphreys, R.M. & McElroy, D.B. 1984, *ApJ*, 284, 565
- Johnson, H. L. 1965, *ApJ*, 141, 923
- Künzli, M., North, P. Kurucz, R.L., & Nicolet, B. 1997, *A&AS*, 122, 51
- Kurucz, R. L. 1991, in *Stellar Atmospheres: Beyond Classical Models*, ed. L. Crivellari, I. Hubeny, & D. G. Hummer (NATO ASI Ser. C.; Dordrecht: Kluwer), 441
- Lesh, J. R. 1968, *ApJS*, 17, 371
- Lindemann, E. 1974, *A&AS*, 15, 209
- Malagnini, M. L., Faraggiana, R., Morossi, C., & Crivellari, L. 1982, *A&A*, 114, 170
- Malagnini, M. L., Faraggiana, R., & Morossi, C. 1983, *A&A*, 128, 375
- Malagnini, M. L., Morossi, C., & Faraggiana, R. 1984, in *The MK Process and Stellar classification*, ed. R.F. Garrison (David Dunlap Observatory:Toronto), 321–375
- Markwardt, C. 2003, <http://astrog.physics.wisc.edu/~craigm/idl/idl.html>
- Massa, D. 1975 *PASP*, 87, 777
- Massa, D. 1987, *AJ*, 94, 1675

- Massa, D. & Fitzpatrick, E. L. 2000, *ApJS*, 126, 517
- Massa, D. & Fitzpatrick, E. L. 2004, in *Astrophysics of Dust*, eds. A. Witt, B. Draine, and G. Clayton, ASP Conference Series, Volume 309, 795
- Matsushima, S. 1969, *ApJ*, 158, 1137
- Mermilliod, J.-C., Mermilliod, M., & Hauck, B. 1997 *A&A*, 124, 349
- Moon, T. T., & Dworetsky, M. M. 1985, *MNRAS*, 217, 305
- Napiwotzki, R., <http://www.astro.le.ac.uk/rn38/uvbybeta.html>
- Napiwotzki, R., Schönberner, D., & Wenske, V. 1993, *A&A*, 268, 653
- Nichols, J. S. & Linsky, J. L. 1996, *AJ*, 111, 517
- Nicolet, B. 2004, private communication.
- Niemczura, E. 2003, *A&A*, 404, 689
- Panagia, N. 1973, *AJ*, 78, 929
- Perryman, M. A. C., Lindegren, L., Kovalevsky, J., Hoeg, E., Bastian, U., Bernacca, P. L., Crèze, M., Donati, F., Grenon, M., van Leeuwen, F., van der Marel, H., Mignard, F., Murray, C. A., Le Poole, R. S., Schrijver, H., Turon, C., Arenou, F., Froeschlè, M., & Petersen, C. S. 1997 *A&A*, 323, 49P
- Qiu, H. M., Zhao, G., Chen, Y. Q., & Li, Z. W. 2001, *ApJ*, 548, 953
- Relyea, L. J. & Kurucz, R. L. 1978, *ApJS*, 37, 45
- Repolust, T., Puls, J., & Herrero, A. 2004, *A&A*, 414,349
- Ribas, I., Guinan, E. F., Fitzpatrick, E. L., DeWarf, L. E., Maloney, F. P., Maurone, P. A., Bradstreet, D. H., Giménez, Á. & Pritchard, J. D. 2000, *ApJ*, 528, 692
- Ribas, I., Fitzpatrick, E. L., Maloney, F. P., Guinan, E. F. & Udalski, A. 2002, *ApJ*, 574, 771
- Rufener, F. 1981, *A&AS*, 45, 207
- Schaller, G., Schaerer, D., Meynet, G., & Maeder, A. 1992, *A&AS*, 96, 269
- Schmidt-Kaler, Th. 1982, in *Landolt-Bornstein, Numerical Data and Functional Relationships in Science and Technology*, Vol. 2, eds. K. Schaifers & H.H. Voigt (Springer Verlag:Berlin), 451
- Smith, K. C., & Dworetsky, M. M. 1993, */aap*, 274, 335
- Strömgren, B. 1966 *ARA&A*, 4, 433

Townsend, R.H.D., Owocki, S.P., & Howarth, I.D. 2004, *MNRAS*, 350, 189

Wenske, V. & Schönberner, D. 1993, in *Inside the stars* (ASP Conf. Series: San Francisco, Vol. 40), ed. W. W. Weiss & A. Baglin, 162

Table 1. Basic Data for Program Stars

HD Number	Star Name	<i>Hipparcos</i> Distance ^a	$v \sin i^b$ (km s ⁻¹)	Spectral Type	Spectral Type Reference ^c
886	γ Peg	102.1 \pm 8.2	5	B2 IV	6
9132	48 Cet	67.9 \pm 3.4	20	A1 Va	3
10250	42 Cas	86.1 \pm 4.3	125	B9 V	2
21790	17 Eri	116.7 \pm 10.5	85	B9 III	4
29646	...	102.7 \pm 9.2	120	A1 IV	3
32630	η Aur	67.2 \pm 3.4	125	B3 V	6
38899	134 Tau	83.3 \pm 5.8	25	B9 IV	4
45557	...	88.0 \pm 3.5	...	A0 V	1
47105	γ Gem	32.1 \pm 2.2	30	A1 IVs	3
58142	21 Lyn	76.3 \pm 4.6	10	A0mA1 IV	3
61831	...	176.1 \pm 14.1	180	B2.5 V	5
66591	...	166.1 \pm 13.3	50	B3 V	5
77002	...	190.5 \pm 17.1	50	B2 IV-V	5
79447	...	153.1 \pm 10.7	10	B3 III	5
87901	α Leo	23.8 \pm 0.5	330	B8 Vnn	4
93194	...	148.4 \pm 10.4	295	B4 IVn	5
98664	σ Leo	65.6 \pm 3.3	65	A0 III+	3
103287	γ UMa	25.6 \pm 0.5	170	A0 Van	3
106911	β Cha	83.0 \pm 3.3	260	B5 Vn	5
115823	...	121.4 \pm 9.7	80	B6 V	5
121263	ζ Cen	117.9 \pm 10.6	225	B2.5 IV	5
121743	ϕ Cen	142.7 \pm 14.3	115	B2 IV	5
121790	ν^1 Cen	128.0 \pm 11.5	150	B2 IV-V	5
125238	ι Lup	107.9 \pm 8.6	235	B2.5 IV	5
129116	...	93.5 \pm 6.5	185	B3 V	5
147394	τ Her	96.4 \pm 4.8	30	B5 IV	6
153808	ϵ Her	49.9 \pm 1.5	85	A0 IV+	3
158094	δ Ara	57.4 \pm 2.3	255	B8 IVn	4
160762	ι Her	152.0 \pm 13.7	10	B3 IV	6
172167	α Lyr	7.8 \pm 0.0	15	A0 Va	3
177724	ζ Aql	25.5 \pm 0.5	345	A0 Vann	3
182255	3 Vul	123.5 \pm 9.9	40	B6 III	6
188665	23 Cyg	195.7 \pm 19.6	145	B5 V	6
192907	κ Cep	100.3 \pm 5.0	20	B9 IV+	4
193432	ν Cap	83.5 \pm 6.7	15	B9.5 Va+	3
196867	α Del	73.8 \pm 3.7	155	B9 IV	4
199081	57 Cyg	153.6 \pm 13.8	85	B5 V	6
201908	...	126.4 \pm 7.6	225	B8 Vn	2
210419	...	111.1 \pm 10.0	370	A0 IVnn	3
214923	ζ Peg	63.9 \pm 3.2	185	B8.5 III	4

Table 1—Continued

HD Number	Star Name	<i>Hipparcos</i> Distance ^a	$v \sin i^b$ (km s ⁻¹)	Spectral Type	Spectral Type Reference ^c
215573	ξ Oct	136.1 ± 8.2	50	B6 IV	5
218045	α Peg	42.8 ± 1.3	150	A0 III-IV	3
222439	κ And	52.0 ± 1.6	190	B9 IVn	4
222661	ω^2 Aqr	47.3 ± 1.9	145	B9.5 IV	3
225132	2 Cet	69.9 ± 4.2	190	B9 IVn	4

^aFrom the *Hipparcos* Catalog: Perryman et al. 1997

^b $v \sin i$ values from Glebocki & Stawikowski 2000

^cSpectral type references: (1) Hoffleit 1982; (2) Cowley et al. 1969; (3) Gray & Garrison 1987; (4) Garrison & Gray 1987; (5) Hilter, Garrison, & Schild 1969; (6) Lesh 1968

Table 2. Johnson and Strömgen Photometry

Star	V	$B - V$	$U - B$	$V - R$	$R - I$	J	H	K	$b - y$	$m1$	$c1$	β
HD 886	2.83	-0.22	-0.86	-0.10	-0.18	3.34	...	3.52	-0.11	0.09	0.12	2.627
HD 9132	5.12	0.02	0.05	0.01	0.16	1.09	2.901
HD 10250	5.18	-0.04	-0.02	0.15	1.02	...
HD 21790	4.73	-0.09	-0.26	-0.01	-0.08	-0.04	0.11	0.83	2.761
HD 29646	5.74	-0.02	0.03	-0.01	0.17	1.04	2.909
HD 32630	3.17	-0.18	-0.67	-0.05	-0.18	3.55	3.61	3.68	-0.09	0.10	0.32	2.683
HD 38899	4.90	-0.07	-0.17	0.02	-0.08	-0.03	0.14	0.91	2.825
HD 45557	5.79	0.00	-0.01	0.17	1.03	2.891
HD 47105	1.93	0.00	0.05	0.05	-0.01	1.90	1.88	1.87	0.01	0.15	1.19	2.865
HD 58142	4.61	-0.01	-0.01	-0.01	-0.05	0.00	0.14	1.12	2.875
HD 61831	4.84	-0.19	-0.65	-0.08	-0.16	-0.08	0.11	0.30	2.669
HD 66591	4.81	-0.17	-0.62	-0.04	-0.20	-0.08	0.10	0.31	2.678
HD 77002	4.91	-0.18	-0.74	-0.09	-0.24	-0.09	0.10	0.21	2.659
HD 79447	3.97	-0.19	-0.67	-0.05	-0.18	-0.08	0.10	0.30	2.659
HD 87901	1.36	-0.11	-0.36	-0.02	-0.10	1.56	1.58	1.62	-0.04	0.10	0.71	2.723
HD 93194	4.82	-0.14	-0.62	-0.01	-0.14	-0.06	0.10	0.36	2.668
HD 98664	4.04	-0.06	-0.11	-0.02	0.13	1.01	2.827
HD 103287	2.44	0.00	0.01	0.00	-0.04	2.40	...	2.37	0.01	0.16	1.11	2.885
HD 106911	4.24	-0.13	-0.52	-0.02	-0.11	-0.05	0.10	0.45	2.710
HD 115823	5.47	-0.13	-0.53	-0.08	-0.15	-0.07	0.12	0.46	2.734
HD 121263	2.54	-0.23	-0.90	-0.14	-0.20	3.09	...	3.29	-0.11	0.08	0.05	2.619
HD 121743	3.82	-0.22	-0.83	-0.13	-0.22	-0.10	0.08	0.14	2.635
HD 121790	3.86	-0.21	-0.80	-0.14	-0.21	4.37	4.48	4.52	-0.10	0.09	0.16	2.640
HD 125238	3.55	-0.18	-0.72	-0.10	-0.14	-0.08	0.09	0.25	2.650
HD 129116	3.99	-0.17	-0.69	-0.11	-0.15	-0.08	0.09	0.25	2.672
HD 147394	3.90	-0.15	-0.56	-0.09	-0.17	-0.06	0.09	0.44	2.702
HD 153808	3.92	-0.02	-0.10	-0.01	-0.04	-0.00	0.15	0.92	2.861
HD 158094	3.60	-0.10	-0.30	-0.04	0.10	0.78	2.772
HD 160762	3.80	-0.18	-0.70	-0.10	-0.17	-0.06	0.08	0.29	2.661
HD 172167	0.03	-0.00	-0.01	-0.04	-0.02	0.02	0.00	0.02	0.00	0.16	1.09	2.903
HD 177724	2.99	0.01	0.01	0.01	0.00	0.01	0.15	1.08	2.875
HD 182255	5.19	-0.12	-0.52	-0.04	-0.16	-0.05	0.11	0.49	2.736
HD 188665	5.14	-0.13	-0.55	-0.06	0.10	0.45	2.715
HD 192907	4.38	-0.05	-0.11	-0.02	-0.06	-0.02	0.13	1.03	2.825
HD 193432	4.75	-0.05	-0.10	0.01	-0.06	4.84	4.90	4.85	-0.02	0.13	1.01	2.852
HD 196867	3.77	-0.06	-0.21	0.00	-0.04	-0.02	0.12	0.89	2.796
HD 199081	4.77	-0.14	-0.58	-0.07	-0.13	5.09	5.12	5.16	-0.05	0.10	0.40	2.713
HD 201908	5.91	-0.07	-0.24	-0.04	0.13	0.80	2.805
HD 210419	6.26	-0.01	-0.07	-0.00	0.14	1.07	2.842
HD 214923	3.40	-0.09	-0.24	-0.04	-0.07	-0.04	0.11	0.87	2.768
HD 215573	5.33	-0.15	-0.49	-0.07	0.11	0.51	2.718
HD 218045	2.48	-0.04	-0.04	0.01	-0.03	2.52	...	2.54	-0.01	0.13	1.13	2.838
HD 222439	4.14	-0.07	-0.23	-0.01	-0.07	-0.04	0.13	0.83	2.833
HD 222661	4.48	-0.04	-0.12	0.02	-0.05	-0.02	0.14	0.92	2.870
HD 225132	4.55	-0.05	-0.08	0.03	-0.04	-0.01	0.12	1.02	2.791

Note. — The Johnson and Strömgren data were collected from the General Catalog of Photometric Data maintained by Institute of Astronomy of the University of Lausanne (Switzerland).

Table 3. Geneva Photometry

Star	$U - B$	$V - B$	$B1 - B$	$B2 - B$	$V1 - B$	$G - B$
HD 886	0.39	1.23	0.79	1.63	1.93	2.48
HD 9132	1.52	0.93	0.89	1.50	1.62	2.12
HD 10250	1.42	0.98	0.87	1.51	1.67	2.18
HD 21790	1.16	1.07	0.83	1.55	1.76	2.28
HD 29646
HD 32630	0.63	1.17	0.81	1.60	1.87	2.41
HD 38899	1.28	1.05	0.86	1.54	1.74	2.27
HD 45557	1.46	0.97	0.88	1.51	1.67	2.17
HD 47105	1.60	0.96	0.89	1.52	1.66	2.15
HD 58142	1.50	0.97	0.87	1.50	1.66	2.16
HD 61831	0.59	1.18	0.80	1.60	1.86	2.41
HD 66591	0.62	1.15	0.80	1.58	1.85	2.38
HD 77002	0.51	1.18	0.79	1.59	1.86	2.41
HD 79447	0.59	1.18	0.79	1.59	1.87	2.40
HD 87901	1.05	1.09	0.83	1.57	1.79	2.31
HD 93194	0.66	1.13	0.80	1.58	1.82	2.34
HD 98664	1.36	1.03	0.85	1.52	1.73	2.24
HD 103287	1.54	0.95	0.89	1.51	1.66	2.15
HD 106911	0.78	1.11	0.81	1.56	1.80	2.32
HD 115823	0.78	1.12	0.82	1.56	1.80	2.33
HD 121263	0.32	1.24	0.78	1.62	1.93	2.49
HD 121743	0.39	1.22	0.78	1.61	1.90	2.46
HD 121790	0.42	1.22	0.79	1.61	1.90	2.46
HD 125238	0.54	1.18	0.80	1.61	1.88	2.42
HD 129116	0.54	1.16	0.80	1.59	1.86	2.41
HD 147394	0.75	1.15	0.81	1.58	1.84	2.37
HD 153808	1.37	0.99	0.89	1.52	1.68	2.19
HD 158094	1.09	1.08	0.82	1.55	1.77	2.29
HD 160762	0.59	1.17	0.80	1.60	1.86	2.40
HD 172167	1.50	0.96	0.90	1.51	1.66	2.17
HD 177724	1.51	0.94	0.89	1.51	1.64	2.13
HD 182255	0.81	1.11	0.82	1.56	1.80	2.33
HD 188665	0.76	1.10	0.82	1.58	1.82	2.33
HD 192907	1.38	1.01	0.86	1.54	1.72	2.23
HD 193432	1.38	1.01	0.86	1.52	1.70	2.21
HD 196867	1.25	1.03	0.85	1.54	1.73	2.23
HD 199081	0.72	1.13	0.81	1.58	1.82	2.36
HD 201908
HD 210419	1.46	0.97	0.87	1.51	1.66	2.15
HD 214923	1.20	1.07	0.83	1.56	1.76	2.28
HD 215573	0.82	1.13	0.81	1.57	1.81	2.35

Table 3—Continued

Star	$U - B$	$V - B$	$B1 - B$	$B2 - B$	$V1 - B$	$G - B$
HD 218045	1.50	1.01	0.87	1.54	1.72	2.22
HD 222439	1.18	1.04	0.85	1.53	1.74	2.26
HD 222661	1.30	1.01	0.88	1.52	1.71	2.22
HD 225132	1.37	1.01	0.85	1.53	1.71	2.21

Note. — The Geneva data were collected from the General Catalog of Photometric Data maintained by Institute of Astronomy of the University of Lausanne (Switzerland).

Table 4. 2MASS Photometry

Star	J_{2M}	H_{2M}	K_{2M}
HD 886	3.500 ± 0.264	3.638 ± 0.198	3.770 ± 0.288
HD 9132	5.385 ± 0.248	5.026 ± 0.026	4.963 ± 0.020
HD 10250	5.267 ± 0.286	5.264 ± 0.026	5.215 ± 0.017
HD 21790	5.282 ± 0.228	4.960 ± 0.036	4.886 ± 0.026
HD 29646	5.682 ± 0.019	5.726 ± 0.017	5.705 ± 0.021
HD 32630	3.611 ± 0.262	3.761 ± 0.238	3.857 ± 0.292
HD 38899	5.024 ± 0.290	4.975 ± 0.036	4.983 ± 0.016
HD 45557	5.755 ± 0.018	5.803 ± 0.027	5.754 ± 0.017
HD 47105	1.729 ± 0.244	1.836 ± 0.202	1.917 ± 0.220
HD 58142	4.695 ± 0.234	4.693 ± 0.033	4.572 ± 0.016
HD 61831	5.218 ± 0.037	5.328 ± 0.036	5.338 ± 0.017
HD 66591	5.161 ± 0.037	5.259 ± 0.034	5.260 ± 0.018
HD 77002	5.326 ± 0.043	5.415 ± 0.029	5.413 ± 0.021
HD 79447	4.650 ± 0.248	4.565 ± 0.270	4.441 ± 0.036
HD 87901	1.665 ± 0.314	1.658 ± 0.186	1.640 ± 0.212
HD 93194	5.056 ± 0.017	5.109 ± 0.029	5.094 ± 0.017
HD 98664	4.366 ± 0.302	4.325 ± 0.204	4.139 ± 0.036
HD 103287	2.381 ± 0.290	2.487 ± 0.174	2.429 ± 0.288
HD 106911	4.687 ± 0.206	4.541 ± 0.246	4.556 ± 0.026
HD 115823	5.727 ± 0.032	5.760 ± 0.045	5.802 ± 0.021
HD 121263	3.022 ± 0.254	3.083 ± 0.212	3.220 ± 0.250
HD 121743	4.628 ± 0.282	4.461 ± 0.264	4.491 ± 0.016
HD 121790	4.721 ± 0.214	4.597 ± 0.226	4.469 ± 0.036
HD 125238	3.970 ± 0.228	3.893 ± 0.210	4.102 ± 0.288
HD 129116	4.637 ± 0.244	4.628 ± 0.076	4.487 ± 0.026
HD 147394	3.927 ± 0.210	4.085 ± 0.236	4.285 ± 0.017
HD 153808	3.554 ± 0.174	3.641 ± 0.176	3.916 ± 0.016
HD 158094	3.698 ± 0.232	3.651 ± 0.224	3.710 ± 0.198
HD 160762	4.267 ± 0.270	4.349 ± 0.258	4.228 ± 0.016
HD 172167	-0.177 ± 0.206	-0.029 ± 0.146	0.129 ± 0.186
HD 177724	3.084 ± 0.330	3.048 ± 0.280	2.876 ± 0.360
HD 182255	5.404 ± 0.018	5.480 ± 0.020	5.485 ± 0.022
HD 188665	5.397 ± 0.017	5.468 ± 0.026	5.516 ± 0.034
HD 192907	4.506 ± 0.260	4.418 ± 0.036	4.431 ± 0.017
HD 193432	4.909 ± 0.218	4.856 ± 0.031	4.807 ± 0.016
HD 196867	3.904 ± 0.288	3.890 ± 0.236	3.826 ± 0.015
HD 199081	5.253 ± 0.260	5.105 ± 0.024	5.103 ± 0.016
HD 201908	6.015 ± 0.027	6.108 ± 0.045	6.084 ± 0.024
HD 210419	6.234 ± 0.024	6.314 ± 0.059	6.211 ± 0.016
HD 214923	3.538 ± 0.256	3.527 ± 0.216	3.566 ± 0.274
HD 215573	5.668 ± 0.044	5.649 ± 0.027	5.650 ± 0.020

Table 4—Continued

Star	J_{2M}	H_{2M}	K_{2M}
HD 218045	2.535 ± 0.270	2.744 ± 0.220	2.647 ± 0.306
HD 222439	4.624 ± 0.264	4.595 ± 0.218	4.571 ± 0.354
HD 222661	4.269 ± 0.344	4.622 ± 0.018	4.594 ± 0.018
HD 225132	4.151 ± 0.222	4.610 ± 0.029	4.564 ± 0.017

Note. — The 2MASS data were collected from the NASA/IPAC Infrared Science Archive, which is operated by the Jet Propulsion Laboratory, California Institute of Technology.

Table 5. Best-Fit Parameters for Calibration Stars

Star	T_{eff} (K)	[m/H]	v_{turb} (km/s)	R/R_{\odot}	$E(B - V)$ (mag)	$\log g(Spec)^a$	$\log g(Newton)^b$
HD886	21179 ± 237	0.07 ± 0.10	1.3 ± 0.9	4.80 ± 0.39	0.000	3.98 ± 0.06	3.98
HD9132	9198 ± 46	-0.21 ± 0.09	2.0 ± 0.8	2.39 ± 0.13	0.000	4.04 ± 0.04	4.04
HD10250	10141 ± 61	0.03 ± 0.09	0.3 ± 0.8	2.63 ± 0.13	0.000	3.98 ± 0.04	4.02
HD21790	11548 ± 74	-0.64 ± 0.09	1.6 ± 0.7	3.91 ± 0.34	0.003 ± 0.005	3.78 ± 0.06	3.80
HD29646	9693 ± 68	0.22 ± 0.10	0.0 ± 0.3	2.53 ± 0.24	0.000	3.99 ± 0.07	4.02
HD32630	17201 ± 173	-0.07 ± 0.07	0.0 ± 0.1	3.25 ± 0.18	0.000	4.13 ± 0.04	4.15
HD38899	11089 ± 67	-0.25 ± 0.10	1.5 ± 0.8	2.66 ± 0.18	0.000	4.05 ± 0.05	4.06
HD45557	9595 ± 39	0.05 ± 0.05	0.2 ± 0.5	2.15 ± 0.08	0.000	4.13 ± 0.03	4.90
HD47105	9113 ± 89	0.04 ± 0.14	0.0 ± 0.5	4.95 ± 0.32	0.000	3.53 ± 0.04	3.53
HD58142	9416 ± 47	-0.24 ± 0.11	1.1 ± 0.8	3.30 ± 0.19	0.000	3.83 ± 0.04	3.83
HD61831	17917 ± 293	-0.44 ± 0.42	0.0 ± 0.1	3.86 ± 0.34	0.023 ± 0.009	3.99 ± 0.07	4.04
HD66591	17162 ± 281	-0.11 ± 0.17	0.0 ± 0.2	3.77 ± 0.27	0.011 ± 0.007	4.03 ± 0.05	4.03
HD77002	18773 ± 223	0.07 ± 0.13	0.9 ± 0.7	3.82 ± 0.37	0.000	4.08 ± 0.08	4.08
HD79447	17365 ± 290	0.12 ± 0.21	0.0 ± 0.5	5.03 ± 0.35	0.019 ± 0.007	3.83 ± 0.05	3.83
HD87901	12194 ± 62	-0.37 ± 0.05	0.1 ± 0.7	3.57 ± 0.09	0.000	3.54 ± 0.09	3.89
HD93194	15690 ± 247	-0.33 ± 0.16	0.0 ± 0.0	3.63 ± 0.27	0.010 ± 0.007	3.83 ± 0.09	4.01
HD98664	10220 ± 52	-0.36 ± 0.08	1.0 ± 0.7	3.38 ± 0.16	0.000	3.83 ± 0.03	3.85
HD103287	9336 ± 52	-0.19 ± 0.08	1.8 ± 0.7	3.04 ± 0.08	0.000	3.79 ± 0.03	3.88
HD106911	14495 ± 157	-0.40 ± 0.13	0.5 ± 0.7	2.84 ± 0.13	0.002 ± 0.004	4.03 ± 0.05	4.15
HD115823	14244 ± 173	-0.13 ± 0.15	0.0 ± 0.0	2.38 ± 0.11	0.000	4.26 ± 0.04	4.27
HD121263	23561 ± 283	-0.24 ± 0.10	2.2 ± 0.6	5.80 ± 0.53	0.000	3.84 ± 0.08	3.91
HD121743	21638 ± 388	0.03 ± 0.11	1.2 ± 1.0	4.19 ± 0.35	0.006 ± 0.006	4.08 ± 0.07	4.10
HD121790	21411 ± 377	-0.05 ± 0.12	1.2 ± 1.0	3.74 ± 0.34	0.011 ± 0.007	4.15 ± 0.07	4.18
HD125238	18605 ± 221	0.19 ± 0.15	0.0 ± 0.5	4.05 ± 0.33	0.000	3.94 ± 0.07	4.03
HD129116	18445 ± 344	-0.12 ± 0.13	0.0 ± 0.1	2.93 ± 0.12	0.010 ± 0.008	4.23 ± 0.03	4.27
HD147394	15615 ± 301	0.24 ± 0.18	0.0 ± 0.5	3.55 ± 0.19	0.012 ± 0.007	4.02 ± 0.05	4.03
HD153808	10197 ± 57	-0.13 ± 0.10	0.7 ± 0.8	2.72 ± 0.07	0.000	3.98 ± 0.02	4.00
HD158094	11962 ± 86	-0.62 ± 0.10	1.9 ± 0.7	3.12 ± 0.15	0.000	3.81 ± 0.06	3.98
HD160762	18070 ± 294	-0.22 ± 0.22	0.0 ± 0.0	5.29 ± 0.45	0.032 ± 0.007	3.82 ± 0.06	3.82
HD172167	9549 ± 41	-0.51 ± 0.07	0.0 ± 0.4	2.75 ± 0.03	0.000	3.96 ± 0.01	3.96
HD177724	9308 ± 59	-0.40 ± 0.16	0.0 ± 0.1	2.38 ± 0.06	0.000	3.60 ± 0.14	4.05
HD182255	14650 ± 205	-0.31 ± 0.18	0.8 ± 1.1	2.70 ± 0.19	0.012 ± 0.008	4.19 ± 0.05	4.19
HD188665	14893 ± 214	-0.17 ± 0.16	0.8 ± 0.8	4.30 ± 0.45	0.008 ± 0.006	3.82 ± 0.08	3.86
HD192907	10174 ± 55	-0.32 ± 0.09	0.7 ± 0.7	4.45 ± 0.22	0.000	3.66 ± 0.03	3.66
HD193432	10213 ± 68	-0.08 ± 0.11	0.2 ± 0.7	3.09 ± 0.26	0.000	3.91 ± 0.06	3.91
HD196867	11243 ± 85	-0.49 ± 0.09	1.8 ± 0.7	3.92 ± 0.20	0.022 ± 0.007	3.72 ± 0.04	3.79
HD199081	15484 ± 250	-0.16 ± 0.16	0.0 ± 0.0	3.87 ± 0.36	0.015 ± 0.008	3.95 ± 0.07	3.96
HD201908	11574 ± 58	-0.56 ± 0.06	1.7 ± 0.5	2.45 ± 0.13	0.000	4.03 ± 0.05	4.13
HD210419	9499 ± 75	0.07 ± 0.15	0.0 ± 0.4	2.21 ± 0.20	0.000	3.60 ± 0.18	4.11
HD214923	11190 ± 55	-0.38 ± 0.07	1.6 ± 0.6	4.03 ± 0.22	0.000	3.67 ± 0.05	3.77

Table 5—Continued

Star	T_{eff} (K)	[m/H]	v_{turb} (km/s)	R/R_{\odot}	$E(B - V)$ (mag)	$\log g(Spec)^a$	$\log g(Newton)^b$
HD215573	14347 ± 138	-0.31 ± 0.16	0.8 ± 0.9	2.84 ± 0.20	0.000	4.14 ± 0.05	4.14
HD218045	9765 ± 63	-0.02 ± 0.10	0.2 ± 0.7	4.72 ± 0.14	0.000	3.51 ± 0.03	3.60
HD222439	11361 ± 66	-0.36 ± 0.09	1.6 ± 0.8	2.31 ± 0.09	0.000	4.10 ± 0.03	4.17
HD222661	10504 ± 91	-0.35 ± 0.14	1.5 ± 1.0	1.94 ± 0.06	0.000	4.22 ± 0.03	4.26
HD225132	10291 ± 108	-0.15 ± 0.11	0.0 ± 0.2	2.82 ± 0.16	0.000	3.88 ± 0.05	3.98

^aThe quantity $\log g$ determined using the *ATLAS9* model atmosphere. ^bThe quantity $\log g$ determined using the *ATLAS9* model atmosphere. ^cThe quantity $\log g$ determined using the *ATLAS9* model atmosphere.

^bThe quantity $\log g$ determined using the *ATLAS9* model atmosphere. ^cThe quantity $\log g$ determined using the *ATLAS9* model atmosphere.

Table 6. Sources for Filter Sensitivities Curves

Filter	Source
<i>UBV</i>	Buser & Kurucz (1978)
<i>RIJK</i>	Johnson (1965)
<i>H</i>	Bessell & Brett (1988)
<i>wby</i>	Matsushima (1969)
<i>Geneva</i>	Nicolet (2004)
<i>2MASS</i>	Cutri et al. (2000)

Table 7. Uncertainties in Photometric Transformations

Photometric Index	Actual Transformation Scatter ^a (mag)	Random Errors in Synthetic Photometry ^b (mag)	Implied Mean Observational Error ^c (mag)	Expected Observational Error ^d (mag)
Johnson Photometry				
$U - B$	0.021	0.010	0.018	0.016
$B - V$	0.011	0.005	0.010	0.011
$V - R$	0.026	0.003	0.026	...
$R - I$	0.021	0.004	0.021	...
J	0.013	0.021
H	0.033	0.022	0.025	...
K	0.019	0.023
Strömgren Photometry				
$b - y$	0.006	0.003	0.005	0.008
$m1$	0.008	0.003	0.007	0.011
$c1$	0.019	0.014	0.013	0.012
β	0.012	0.008	0.009	0.010
Geneva Photometry				
$U - B$	0.021	0.014	0.016	0.011
$V - B$	0.013	0.006	0.012	0.008
$B1 - B$	0.008	0.003	0.007	0.008
$B2 - B$	0.007	0.003	0.006	0.008
$V1 - B$	0.012	0.006	0.010	0.008
$G - B$	0.014	0.007	0.012	0.009
<i>2MASS</i> Photometry				
J_{2M}	0.037	0.021	0.030	0.029
H_{2M}	0.058	0.022	0.054	0.036
K_{2M}	0.036	0.023	0.028	0.022

^aStandard deviation of the observed photometry compared with the transformation relations shown in Figures 4 and 5.

^bFor each star, we computed the standard deviations about the mean of the 15 photometric indices from the 100 Monte Carlo SED fits. The values listed are the RMS means (averaged over all the stars) of those standard deviations.

^cMean value of the random photometric errors, computed assuming that the scatter seen in the transformation relations arises from the quadratic sum of the random error in the synthetic photometry and random observational error in the data.

^dExpected errors for Johnson $U - B$ and $B - V$ indices are from the statistical analysis of FitzGerald 1973. Those for the Strömgren system are from Lindemann 1974. Those for the Geneva are derived from the analysis of Rufener 1981. For the *2MASS* magnitudes, the errors listed are the RMS values derived from the actual observational errors for the

stars in our sample. Only the well-determined magnitudes (those with errors less than 0.1 mag) were used in this calculation (see Figure 8).

Table 8a. Synthetic Johnson Photometry for ATLAS9 [m/H] = -1.5, $v_{turb} = 0$ km/s Models [The complete version of this table is in the electronic edition of the Journal. The printed edition contains only a sample.]

T_{eff}	$\log g$	[m/H]	v_{turb}	V	$U - B$	$B - V$	$V - R$	$R - I$	J	H	K
9000.	1.40	-1.5	0.0	-40.234	-0.199	0.008	0.083	0.045	-40.336	-40.371	-40.372
9000.	1.50	-1.5	0.0	-40.243	-0.176	-0.002	0.074	0.044	-40.339	-40.372	-40.372
9000.	2.00	-1.5	0.0	-40.268	-0.090	-0.031	0.048	0.038	-40.346	-40.371	-40.373
9000.	2.50	-1.5	0.0	-40.278	-0.026	-0.033	0.040	0.029	-40.351	-40.371	-40.376
9000.	3.00	-1.5	0.0	-40.281	0.024	-0.017	0.039	0.019	-40.355	-40.371	-40.380

Table 9a. Synthetic Stromgren Photometry for ATLAS9 [m/H] = -1.5, $v_{turb} = 0$ km/s Models
 [The complete version of this table is in the electronic edition of the Journal. The printed edition
 contains only a sample.]

T_{eff}	$\log g$	[m/H]	v_{turb}	$b - y$	$m1$	$c1$	β
9000.	1.40	-1.5	0.0	0.056	0.063	1.133	2.627
9000.	1.50	-1.5	0.0	0.048	0.066	1.184	2.644
9000.	2.00	-1.5	0.0	0.020	0.080	1.326	2.724
9000.	2.50	-1.5	0.0	0.010	0.096	1.352	2.794
9000.	3.00	-1.5	0.0	0.009	0.117	1.310	2.848

Table 10a. Synthetic Geneva Photometry for ATLAS9 [m/H] = -1.5, $v_{turb} = 0$ km/s Models [The complete version of this table is in the electronic edition of the Journal. The printed edition contains only a sample.]

T_{eff}	$\log g$	[m/H]	v_{turb}	$U - B$	$V - B$	$B1 - B$	$B2 - B$	$V1 - B$	$G - B$
9000.	1.40	-1.5	0.0	1.477	0.977	0.826	1.556	1.676	2.157
9000.	1.50	-1.5	0.0	1.520	0.987	0.826	1.557	1.686	2.170
9000.	2.00	-1.5	0.0	1.648	1.012	0.830	1.554	1.710	2.205
9000.	2.50	-1.5	0.0	1.688	1.007	0.843	1.544	1.705	2.202
9000.	3.00	-1.5	0.0	1.677	0.983	0.860	1.527	1.681	2.179

Table 11a. Synthetic 2MASS Photometry for ATLAS9 [m/H] = -1.5, $v_{turb} = 0$ km/s Models [The complete version of this table is in the electronic edition of the Journal. The printed edition contains only a sample.]

T_{eff}	$\log g$	[m/H]	v_{turb}	J_{2M}	H_{2M}	K_{2M}
9000.	1.40	-1.5	0.0	-40.381	-40.383	-40.425
9000.	1.50	-1.5	0.0	-40.384	-40.384	-40.425
9000.	2.00	-1.5	0.0	-40.390	-40.384	-40.426
9000.	2.50	-1.5	0.0	-40.396	-40.383	-40.429
9000.	3.00	-1.5	0.0	-40.401	-40.383	-40.434

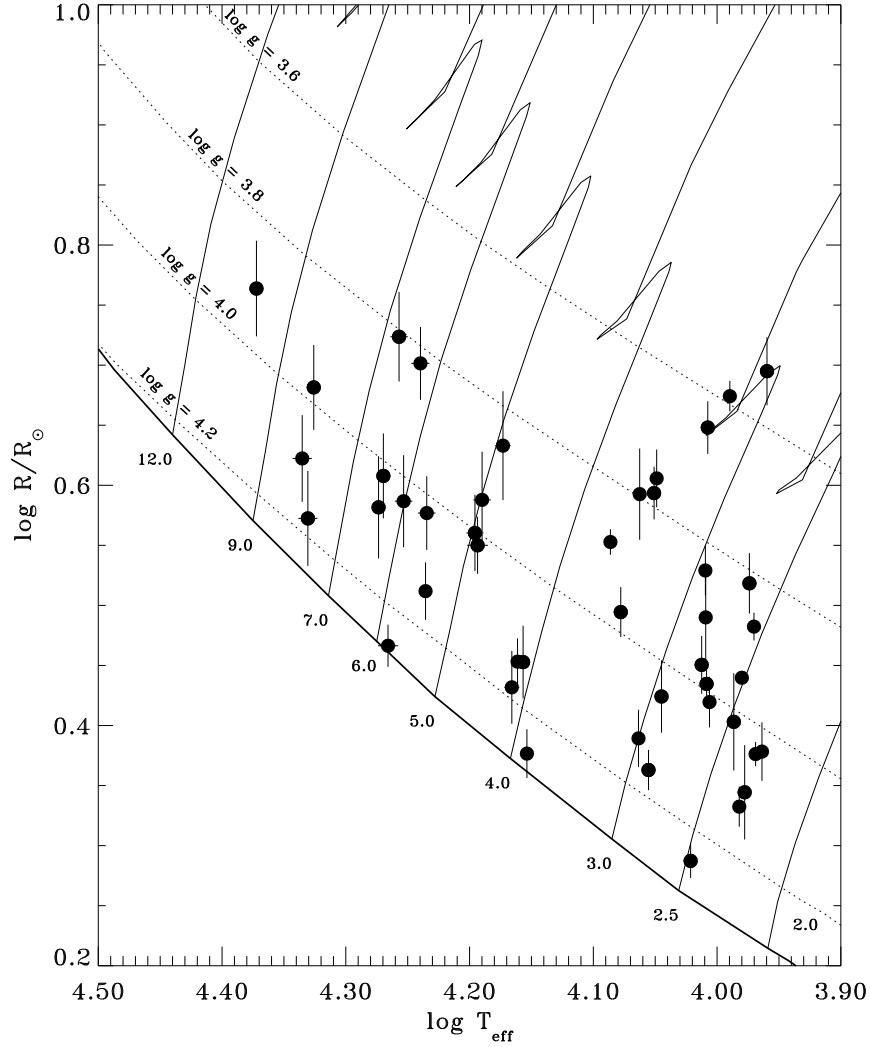


Fig. 1.— Theoretical HR Diagram, expressed in terms of $\log R/R_{\odot}$ vs $\log T_{\text{eff}}$, based on the stellar evolution models of Bressan et al. 1993. The thick solid curve shows the location of the Zero Age Main Sequence (ZAMS) and the thin solid curves show the evolution tracks for the initial stellar masses listed along the ZAMS, in units of M/M_{\odot} . Lines of constant Newtonian surface gravity (i.e., GM/R^2) are shown for several representative and relevant values. The filled circles show the positions of our program stars in the HRD. Note that, for most stars, the error bar for T_{eff} lies within the symbol. The derivation of the stellar properties is discussed in §§ 2 and 4.

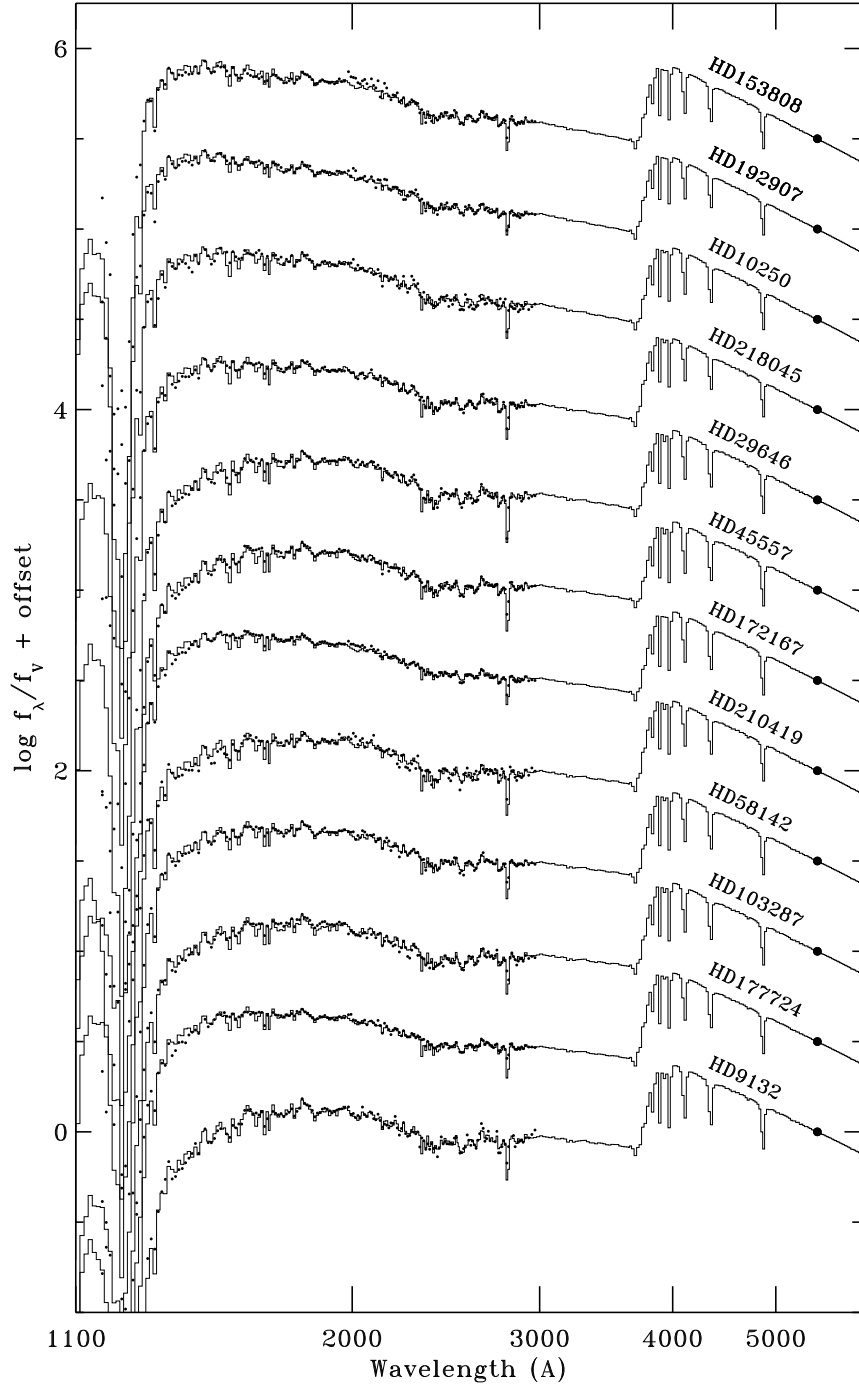


Fig. 2.— Model fits to the observed fluxes of the program stars. The solid histogram-style curves are the best fitting models (reddened to match the observations). The points are the observed *IUE* data and *V* magnitudes. The x-axis is a logarithmic wavelength scale. The y-axis is $\log f_\lambda/f_V$, with each star offset for display purposes. Each tick mark on the ordinate is 0.5 dex. Each star is labeled with its HD number. The fits are arranged so that T_{eff} increases upward in each plot and with each subsequent plot.

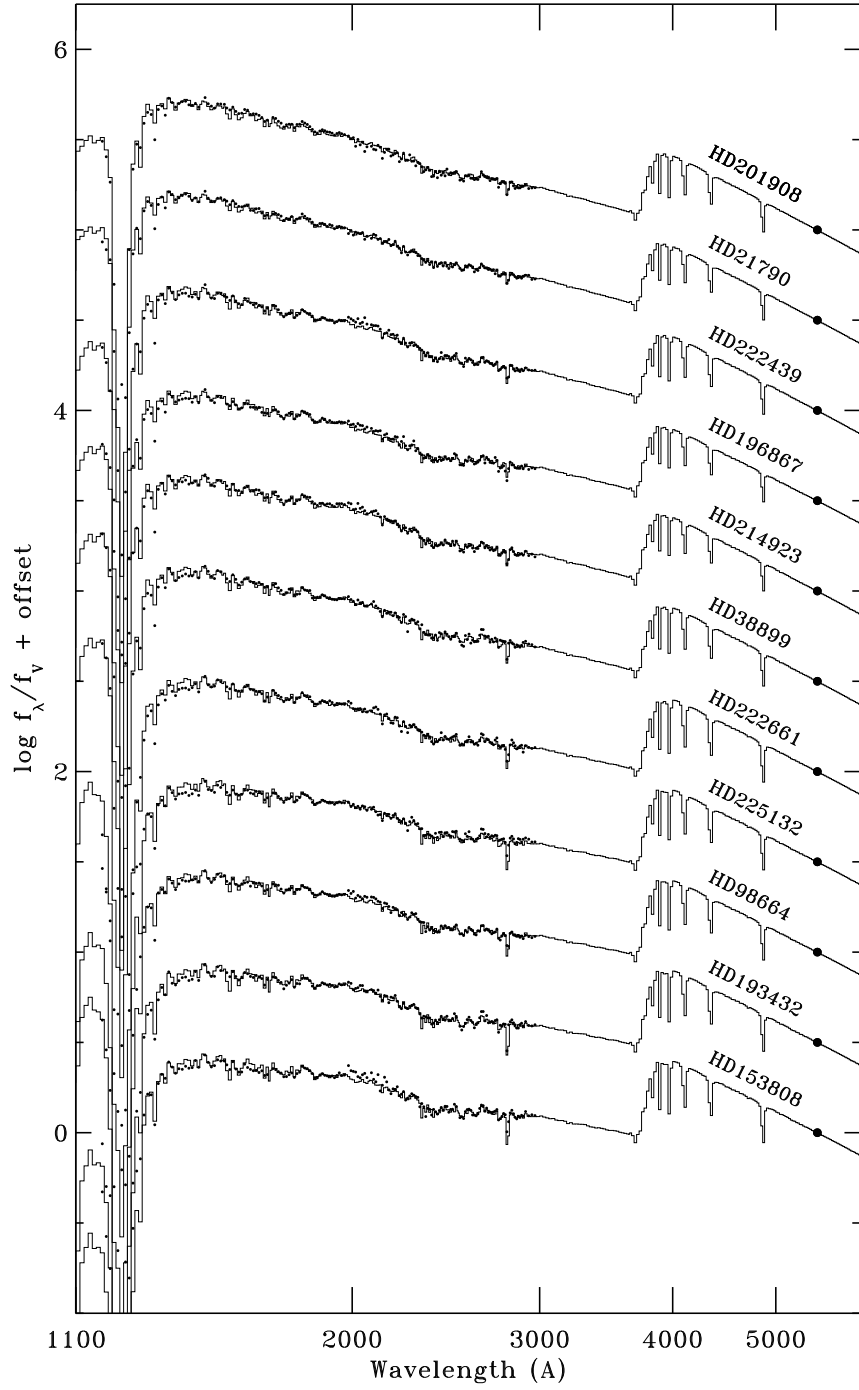


Fig. 2.— Figure 2 continued

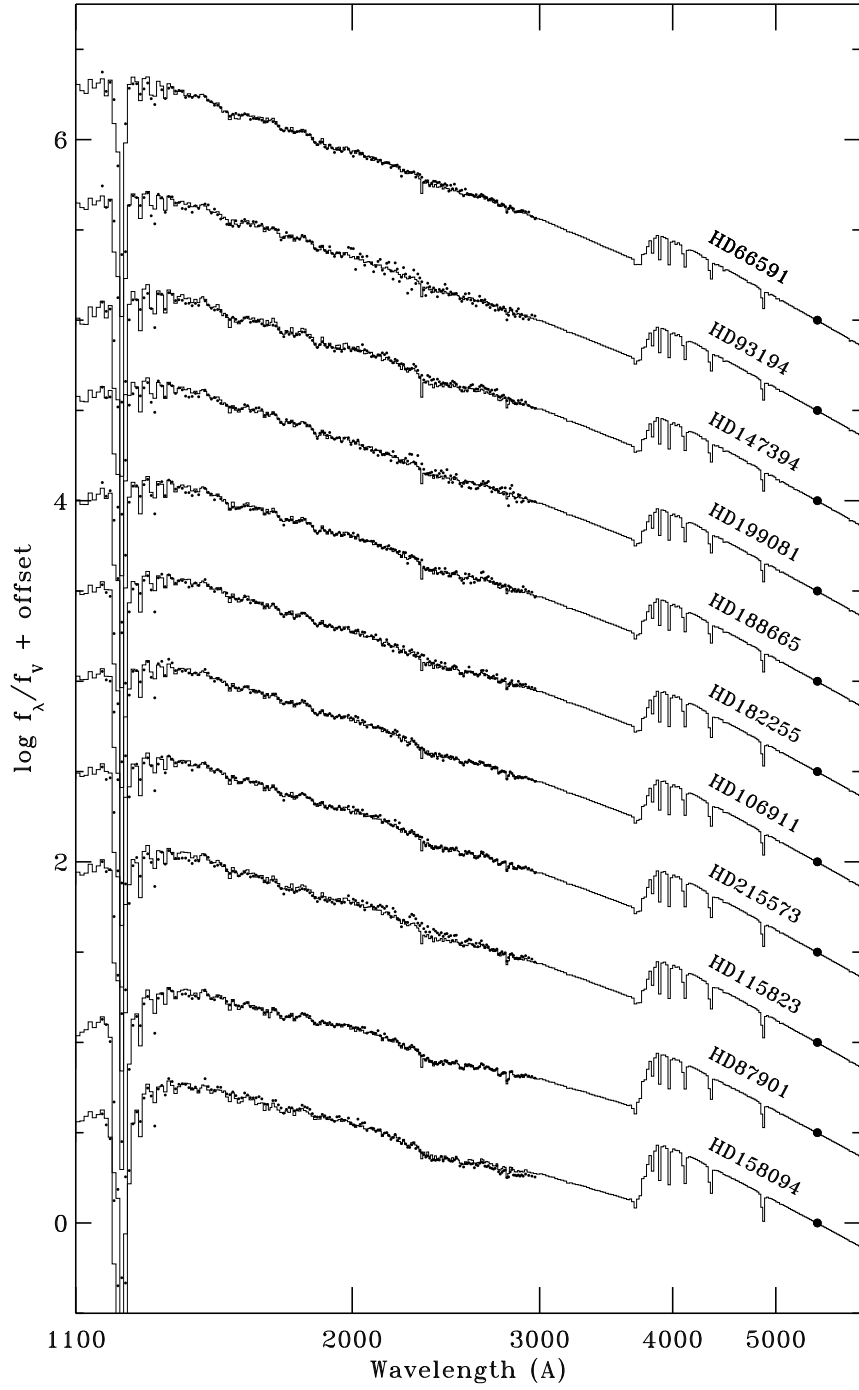


Fig. 2.— Figure 2 continued

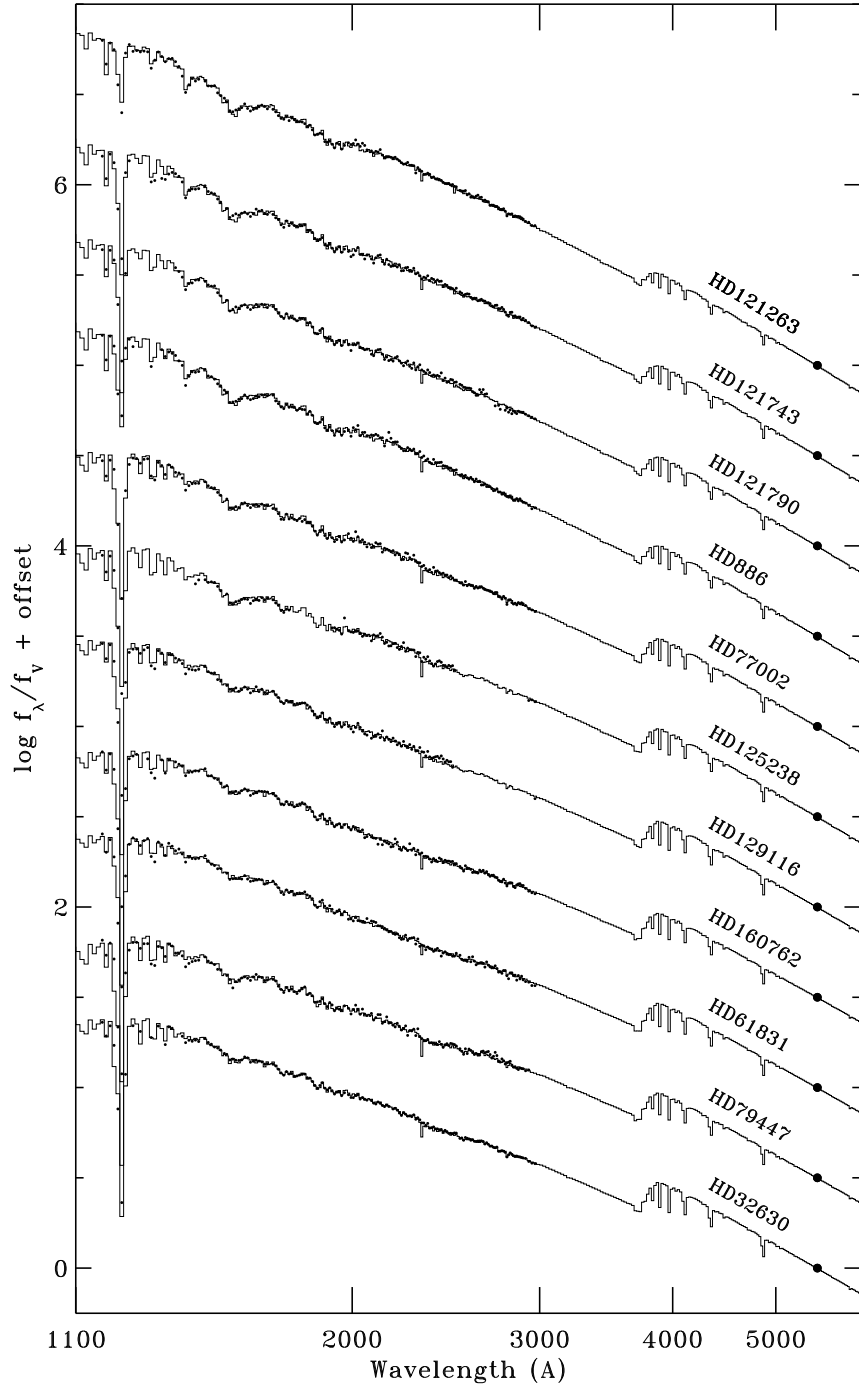


Fig. 2.— Figure 2 continued

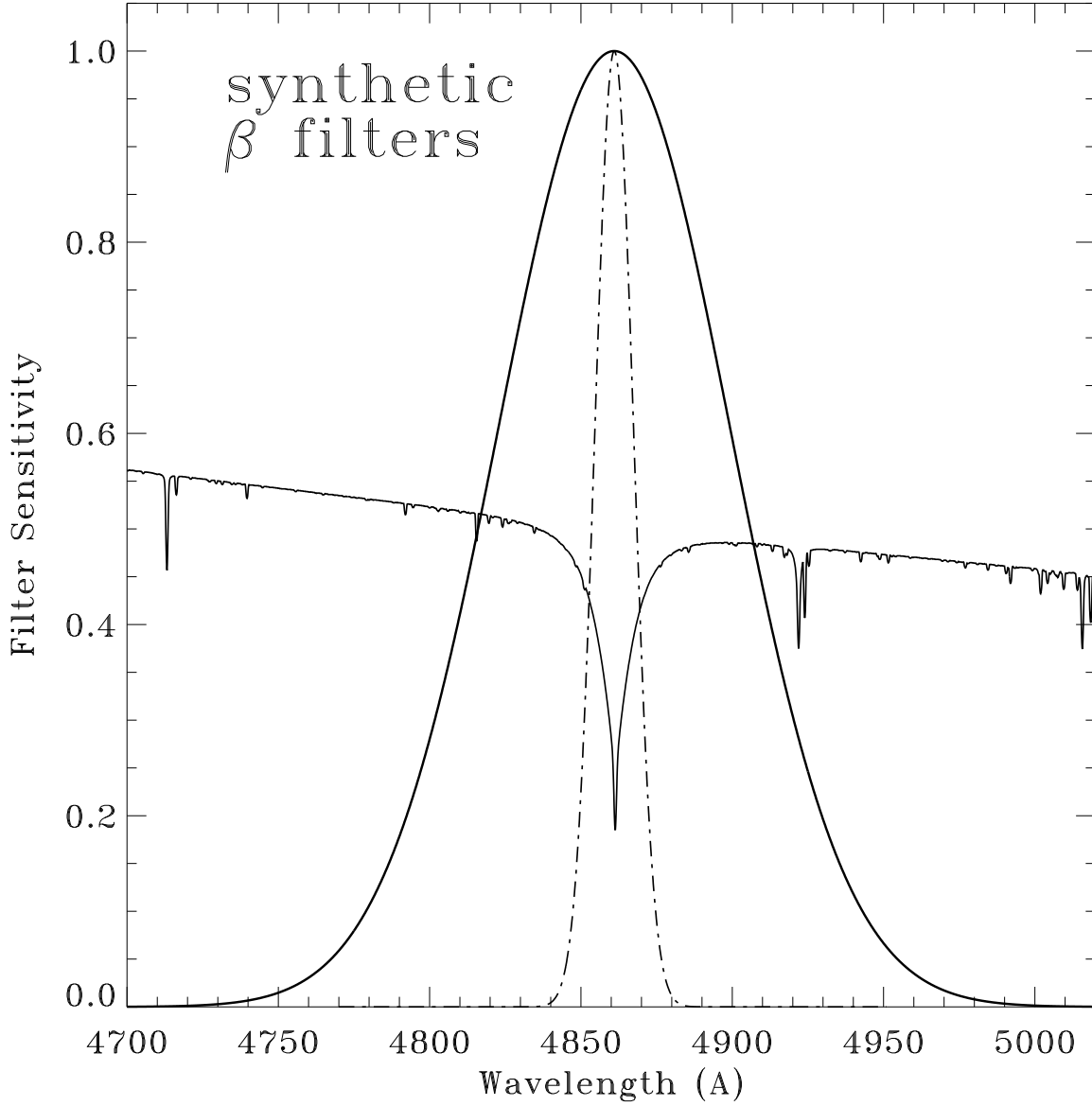


Fig. 3.— The adopted models for the β filter profiles, compared with a synthetic spectrum for a typical B star ($T_{eff} = 15000$ K, $\log g = 4$, $[m/H] = 0.0$, $v_{turb} = 2$ km s $^{-1}$). The intermediate (solid curve) and narrow (dash-dot curve) β filters are represented by Gaussians with FWHM values of 90 Å and 15 Å, respectively. The β index is the difference between the magnitudes measured by the two filters. We perform the synthetic photometry with the filters scaled to maximum values of 1.0, as shown in the figure.

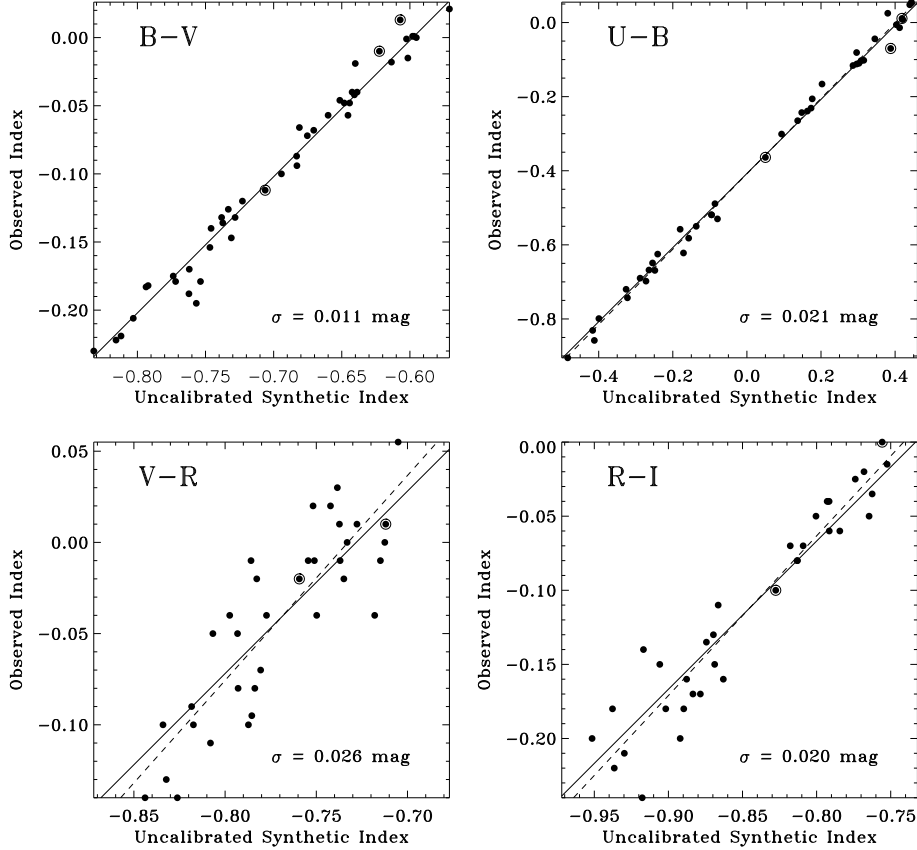


Fig. 4.— Filter calibration relations for Johnson photometric indices. Each panel shows the relationship between the uncalibrated synthetic indices and the observed indices for the 45 calibration stars. In all the panels, the solid lines have a slope of unity and show the simple mean offset between the observed and synthetic photometry. This provides an adequate calibration for $B - V$, but the other indices require linear calibrations, as indicated by the dashed lines. The adopted relationships between the observed and synthetic indices are as follows: $B - V = 0.598 + (B - V)_{syn}$; $U - B = -0.408 + 1.018(U - B)_{syn}$; $V - R = 0.823 + 1.124(V - R)_{syn}$; and $R - I = 0.799 + 1.078(R - I)_{syn}$. Circled points show the positions of the three most rapid rotators in the sample: HD 87901, HD 177724, and HD 210419. These are discussed in §7.2.

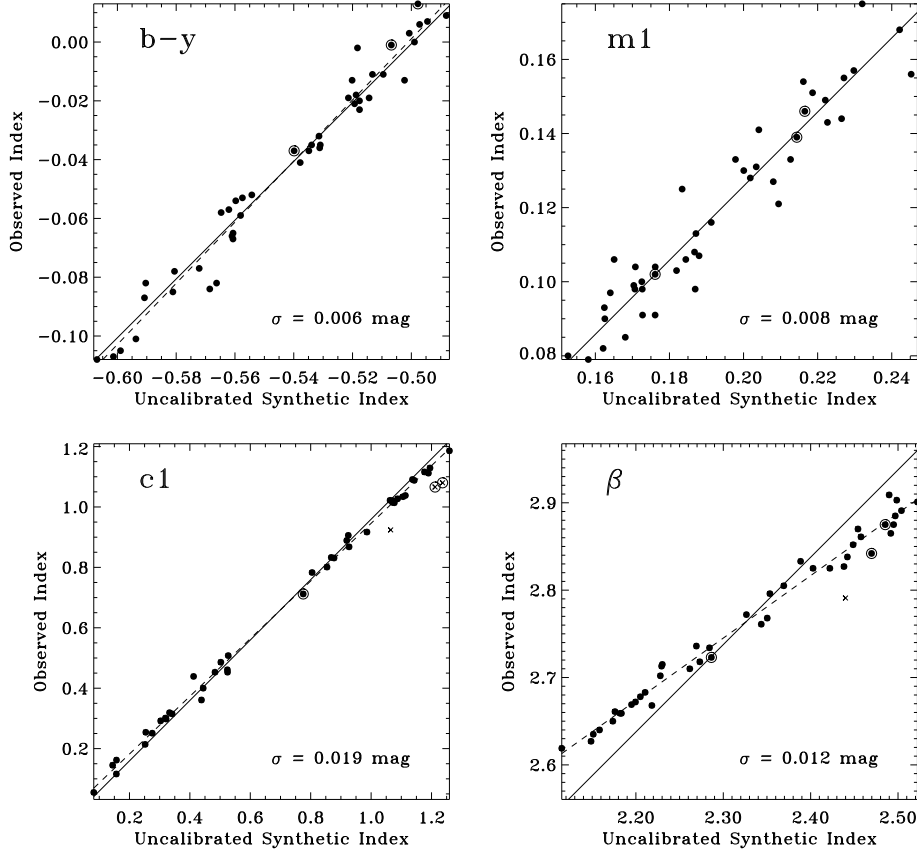


Fig. 5.— Same as Figure 4, but for the Strömgren photometric indices. For $m1$, a simple offset of unity slope provides an adequate calibration (solid line) and is given by $m1 = -0.074 + m1_{syn}$. For $b - y$, $c1$, and β , linear calibrations are adopted (dashed lines), given by: $b - y = 0.521 + 1.040(b - y)_{syn}$; $c1 = -0.009 + 0.955c1_{syn}$; and $\beta = 1.101 + 0.715\beta_{syn}$. In the $c1$ and β panels, the crosses indicate data points excluded from the calibrations, and correspond to the stars HD 158303, HD 177724, and HD 210419 for $c1$ and HD 225132 for β . As in Figure 4, circled points show the positions of the three most rapid rotators in the sample: HD 87901, HD 177724, and HD 210419.

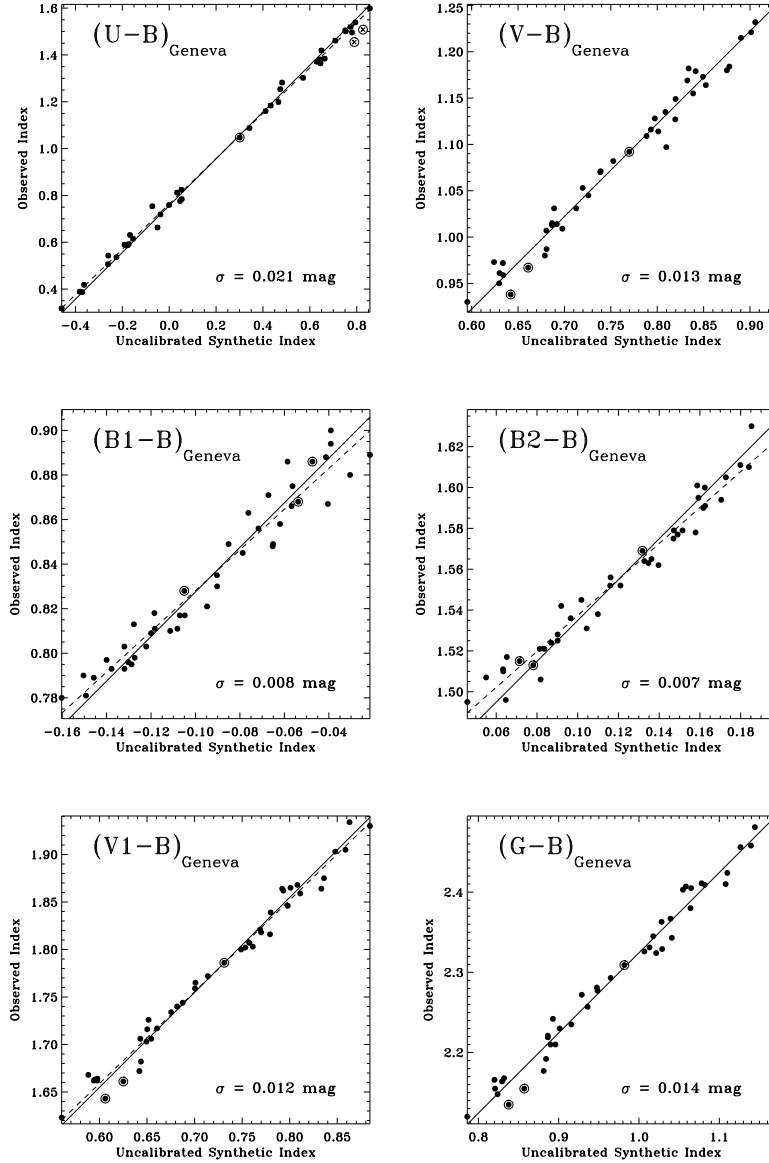


Fig. 6.— Same as Figure 4, but for the Geneva optical colors. For $V - B$ and $G - B$, simple offsets of unity slope provide adequate calibrations (solid lines) and are given by $V - B = 0.322 + (V - B)_{syn}$ and $G - B = 1.324 + (U - B)_{syn}$. For the other indices, linear calibrations are adopted (dashed lines) and are given by $U - B = 0.764 + 0.969(U - B)_{syn}$; $B1 - B = 0.920 + 0.914(B1 - B)_{syn}$; $B2 - B = 1.449 + 0.881(B2 - B)_{syn}$; and $V1 - B = 1.0709 + 0.966(V1 - B)_{syn}$. In the $U - B$ panel, the cross indicates the data points for the stars HD 177724 and HD 210419, which were excluded from the calibration. As in the previous two figures, circled points show the positions of the three most rapid rotators in the sample: HD 87901, HD 177724, and HD 210419.

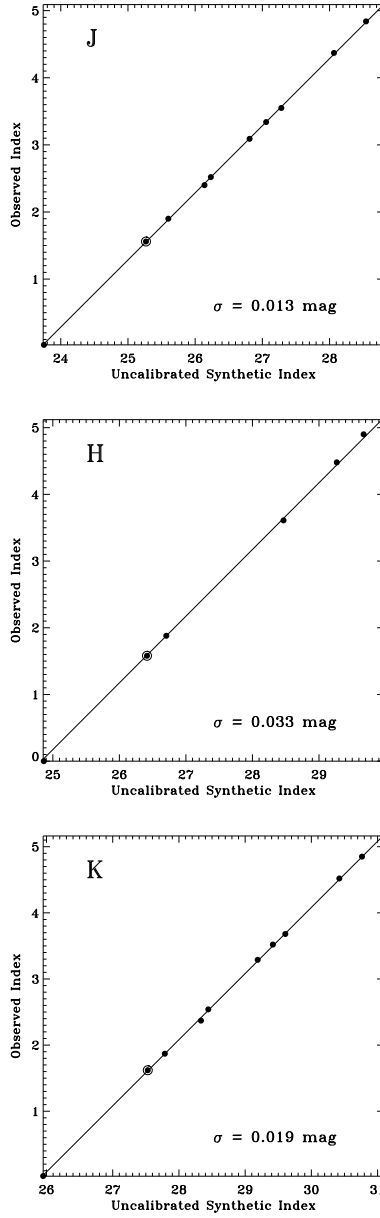


Fig. 7.— Same as Figure 4, but for the Johnson near-IR magnitudes. The relationships between the observed and synthetic values are as follows: $J = -23.715 + J_{syn}$; $H = -24.827 + H_{syn}$; and $K = -25.918 + K_{syn}$. As in the previous three figures, circled points show the positions of the three most rapid rotators in the sample: HD 87901, HD 177724, and HD 210419.

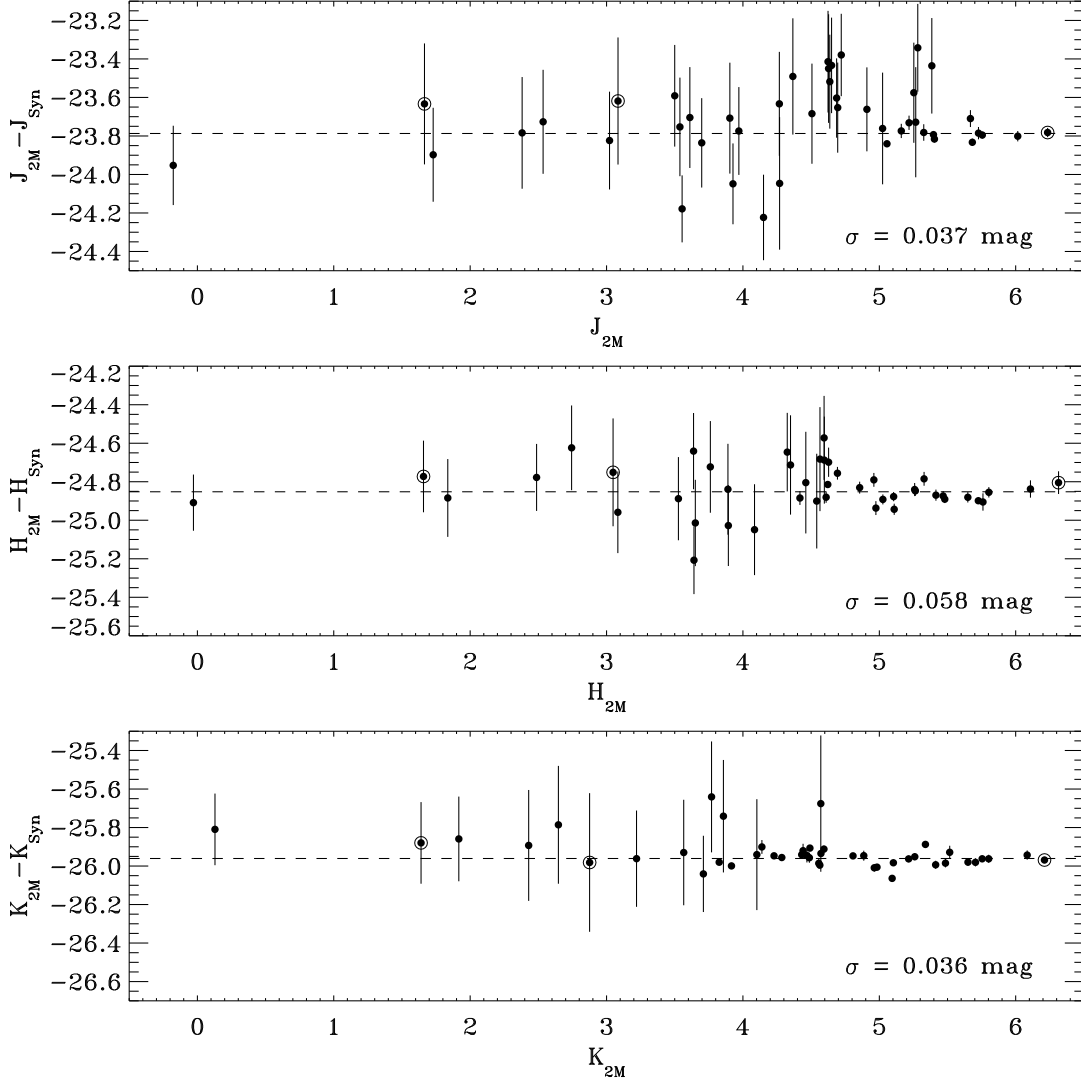


Fig. 8.— Filter calibration relations for *2MASS* photometry. Each panel shows the difference between the observed and synthetic magnitudes, plotted against the observations. Vertical error bars show the individual observational errors, as listed in Table 4. The dashed lines show the simple mean value of the difference, based only on the observations with errors less than 0.1 mag. The mean calibration relations are: $J_{2M} = -23.787 + J_{2Msyn}$; $H_{2M} = -24.852 + H_{2Msyn}$; and $K_{2M} = -25.961 + K_{2Msyn}$. The rms scatter about these relations is also shown in each panel, based only on the data with errors less than 0.1 mag. As in the previous four figures, circled points show the positions of the three most rapid rotators in the sample: HD 87901, HD 177724, and HD 210419.

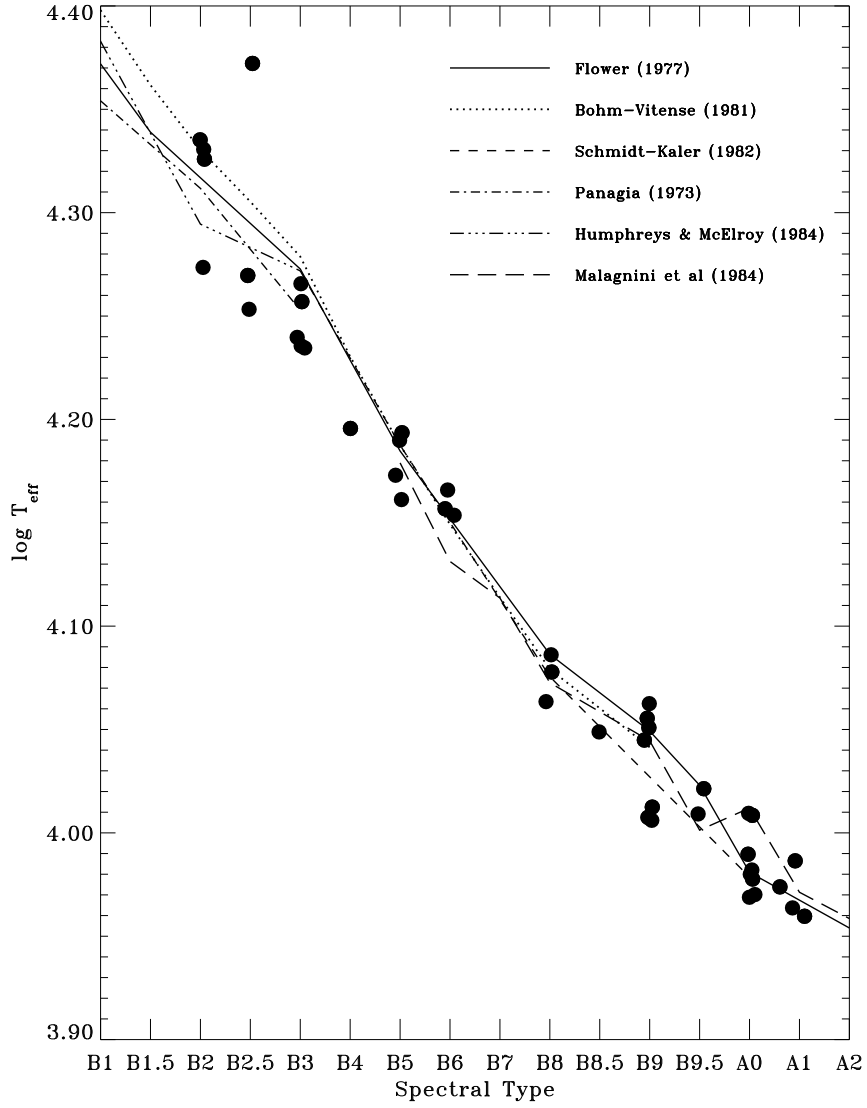


Fig. 9.— $\log T_{eff}$ as a function of spectral type for the program stars (filled circles). The various dotted, dashed, and solid lines show a number of published spectral type vs. T_{eff} calibrations, as indicated in the figure. Small random horizontal offsets have been added to the data points to increase their visibility

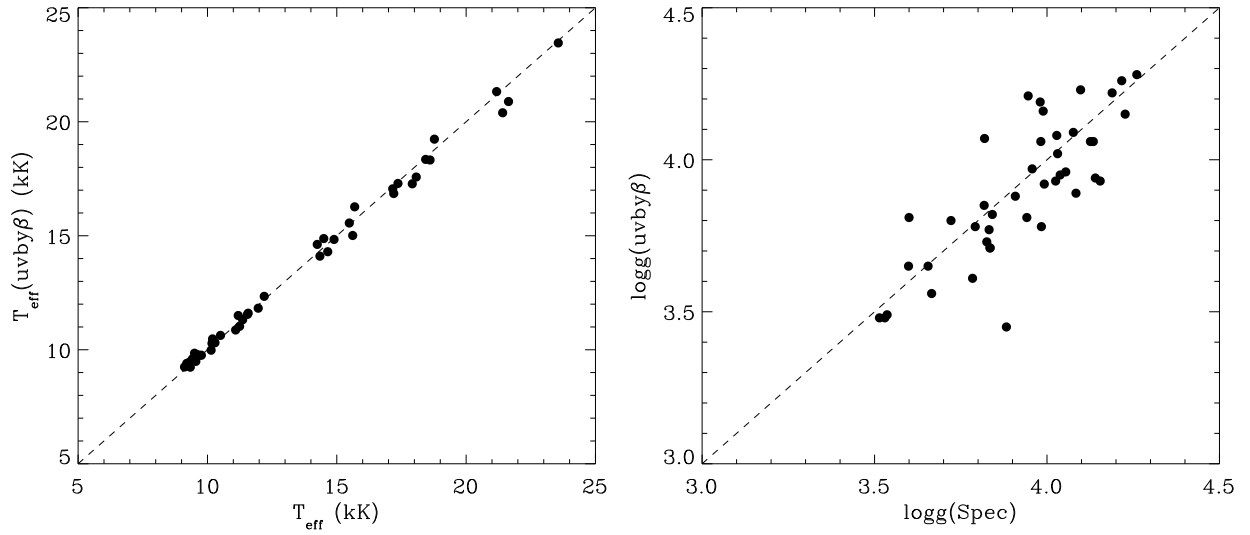


Fig. 10.— Relations between the values of T_{eff} and $\log g$ derived in this paper (see Table 5) plotted against those determined from the observed uvby β photometry and the calibration derived by Napiwotzki et al. (1993). The dashed line in each plot has a slope of unity, indicating exact agreement.

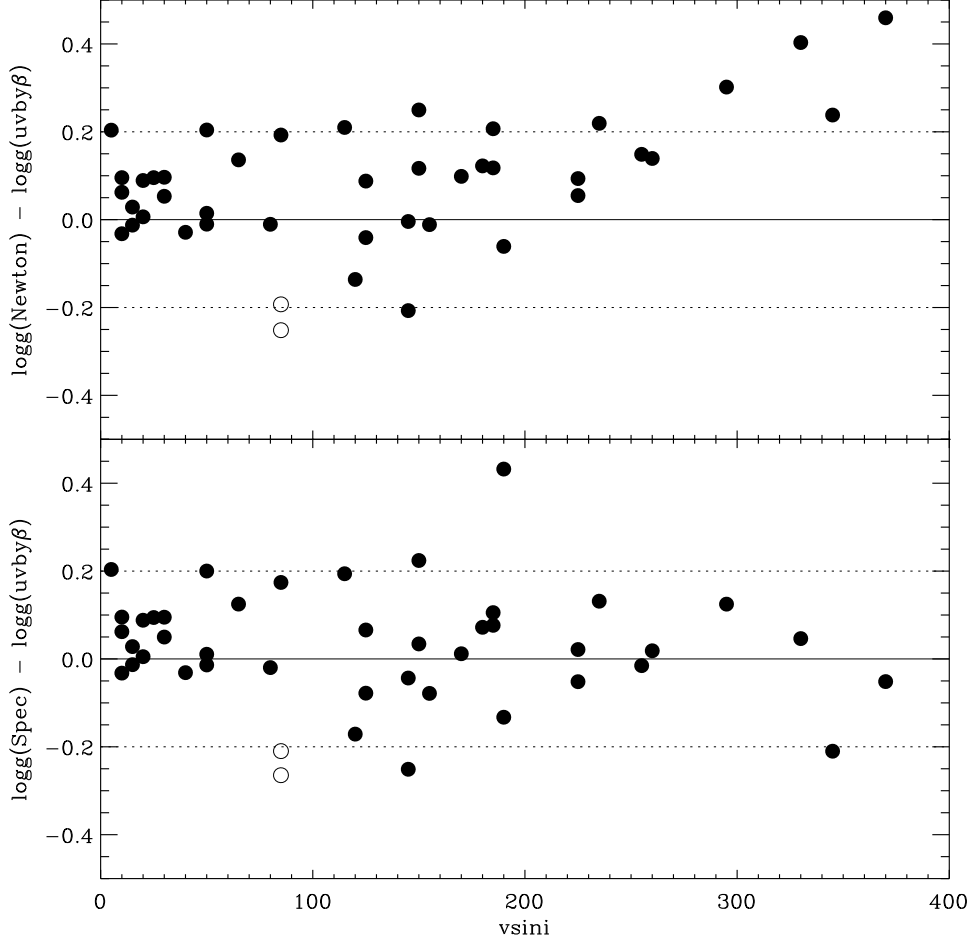


Fig. 11.— Systematic effects in the $\log g$ determinations. The upper panel shows the $v \sin i$ dependence of the differences between Newtonian surface gravities determined from our *Hipparcos*-constrained data and the surface gravities based on $uvby\beta$ photometry. The lower panel shows how this systematic trend is removed by including centrifugal effects in the computation of $\log g(\text{Spec})$ (see Eq. 3). Open symbols are shown for the stars HD 153808 and HD 199081, which are double-line spectroscopic binaries. For such cases, our *Hipparcos*-based approach underestimates the Newtonian gravities by approximately a factor-of-two, accounting for the large negative residuals. The star with the largest positive residual in the lower plot, i.e., HD 225132 at $v \sin i = 190$ km/sec, lies outside the bounds of the upper plot. The dotted lines in each panel at ± 0.2 are provided for visual reference.